

The Formation and Fragmentation of Disks around Primordial Protostars

Paul C. Clark,^{1*} Simon C.O. Glover,¹ Rowan J. Smith,¹ Thomas H. Greif,²
Ralf S. Klessen,^{1,3} Volker Bromm⁴

¹ Institut für theoretische Astrophysik, Zentrum für Astronomie der Universität Heidelberg,
Albert-Ueberle-Str. 2, 69120, Heidelberg, Germany

² Max-Planck-Institut für Astrophysik, Karl-Schwarzschild-Str. 1,
D-85748 Garching, Germany

³ Kavli Institute for Particle Astrophysics and Cosmology,
Stanford University, Menlo Park, CA 94025, USA

⁴ The University of Texas, Department of Astronomy and Texas Cosmology Center,
2511 Speedway, RLM 15.306, Austin, TX 78712, USA

*To whom correspondence should be addressed; E-mail: pcc@ita.uni-heidelberg.de.

The very first stars to form in the universe heralded an end to the cosmic dark ages and introduced new physical processes that shaped early cosmic evolution. Until now, it was thought that these stars lived short, solitary lives, with only one extremely massive star, or possibly a very wide binary system, forming in each dark matter minihalo. Here we describe numerical simulations that show that these stars were, to the contrary, often members of tight multiple systems. Our results show that the disks that formed around the first young stars were unstable to gravitational fragmentation, possibly producing small binary and higher-order systems that had separations as small as the distance between the Earth and the Sun.

The earliest stages of the formation of the first stars in the universe, often termed Population III (Pop III), have been well studied (1–3), with current numerical simulations evolving the collapsing gas from cosmological to protostellar densities (4, 5). Much of the dynamical evolution of the gas during this phase is controlled by the formation of molecular hydrogen, the main coolant of the gas as it is dragged into the collapsing dark matter minihalos. The amount of H₂ formed sets the minimum gas temperature in the minihalos at around 200–300K, resulting in the first self-gravitating baryonic cores – the initial conditions for primordial star formation – having masses of around 1000 times that of the Sun (M_{\odot}).

Until recently, it was assumed that each of these cores formed just a single star, because no fragmentation was seen in the simulations during the formation of the first protostar. As a result, attempts to estimate the final mass of the primordial stars have concentrated on balancing the inward accretion of gas from the collapsing core by the radiative feedback from the young protostar, with various calculations predicting a final mass in the range 30–300 M_{\odot} (1, 5–7).

It has been shown (8) that it is possible for the collapsing baryons to break into two distinct parts, each evolving independently to form its own star, thereby limiting the mass reservoir available for each component. The fragmentation of the gas arises from the chaotic turbulent flows that feed the inner regions of the star-forming minihalos. Numerical simulations suggest that this may occur in about one-fifth of all cases of primordial star formation (8). However this figure is a lower limit, because the simulations were unable to follow the evolution of the gas beyond the formation of the initial protostar or binary system. A different study that followed the evolution of the gas at later times (9) has shown that it settles into a disk with a radius of around 1000 astronomical units (AU), which is unstable to gravitational fragmentation. However, the limited mass resolution of this study, and the fact that it did not include the effects of the radiative feedback from the new-born stars, rendered its results inconclusive

Here, we present the results of a high resolution numerical simulation that captures the

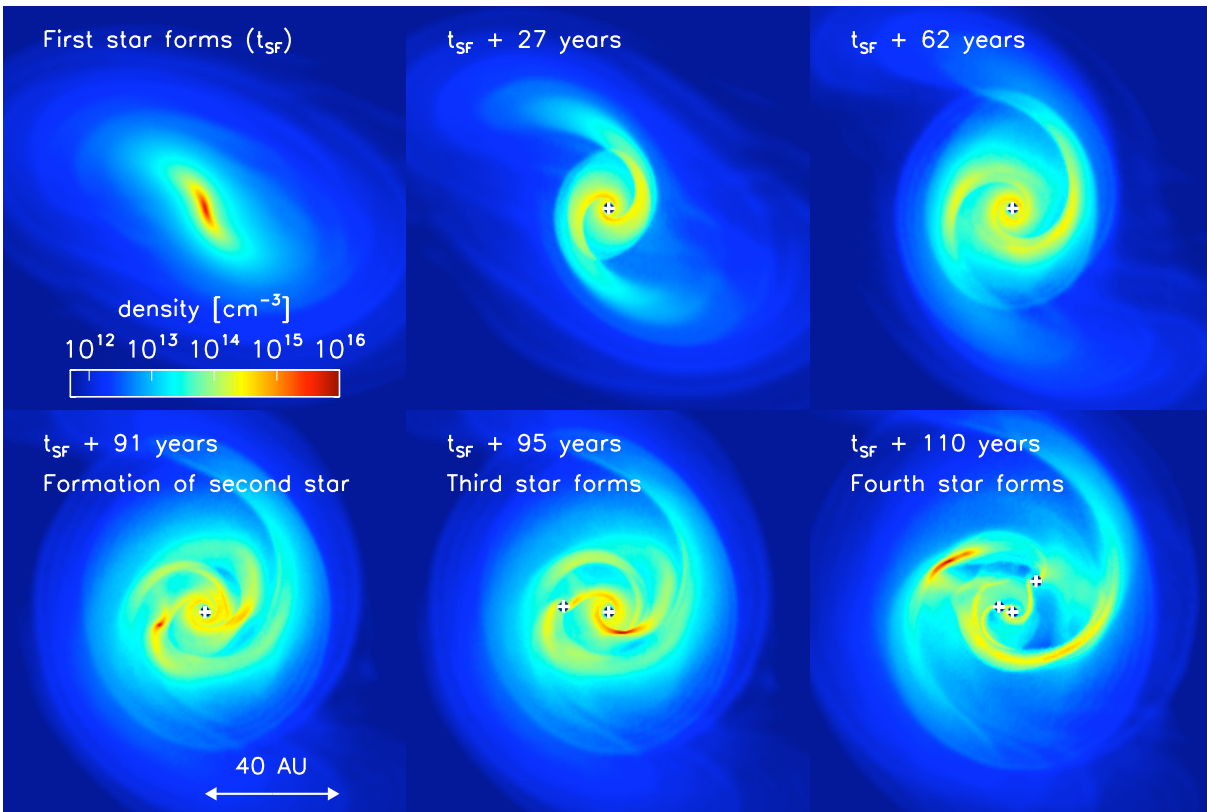


Figure 1: Density evolution in a 120 AU region around the first protostar, showing the build-up of the protostellar disk and its eventual fragmentation. We also see ‘wakes’ in the low-density regions, produced by the previous passage of the spiral arms.

formation of the primordial protostar/disk system from cosmological initial conditions down to scales as small as 1.5 AU, and which includes the effects of the accretion luminosity heating as the disk builds up around the young protostar. We started by identifying the first dark matter minihalo to contain cooling, gravitationally collapsing gas from a simulation of a representative cosmological volume (10).

We then re-zoomed the calculation using a technique called “particle splitting” [employed elsewhere in studies of primordial star formation, e.g. (5)] and we focused our attention only on the collapsing gas at the center of the minihalo, ignoring the larger-scale evolution of the minihalo and its surroundings [see (10) for details]. During this second stage of the simulation, the gas collapsed to very high densities. Normally, numerical simulations of this kind stop once the gas density exceeds around 10^{14} cm^{-3} , because the computational cost of evolving the entire system beyond this point becomes prohibitively expensive. However, in our simulations, we replaced very high density collapsing regions with accreting ‘sink’ particles (10), each of which represents an individual protostar. We then used the measured accretion rate onto the sink particles to calculate the luminosity produced by the mass as it fell onto the young protostar. This energy was then deposited into the surrounding gas under the assumption that the gas is optically thin, thus providing a conservative over-estimate of the heating from the protostar [see (10) for details].

Prior to the formation of the first protostar, the results of our simulation were very similar to those presented elsewhere in the literature (1, 5, 8). However, the use of sink particles allows us to follow the evolution of the gas past the point at which the first protostar forms, and hence to simulate the build-up of an accretion disk around the protostar (Fig. 1).

After around 90 years, the disk had nearly doubled in size. For the first 60 years, the structure of the disk was dominated by a strong two-arm spiral pattern, a feature common to simulations of present-day star formation (11). Spiral structures of this kind are a signature of self-

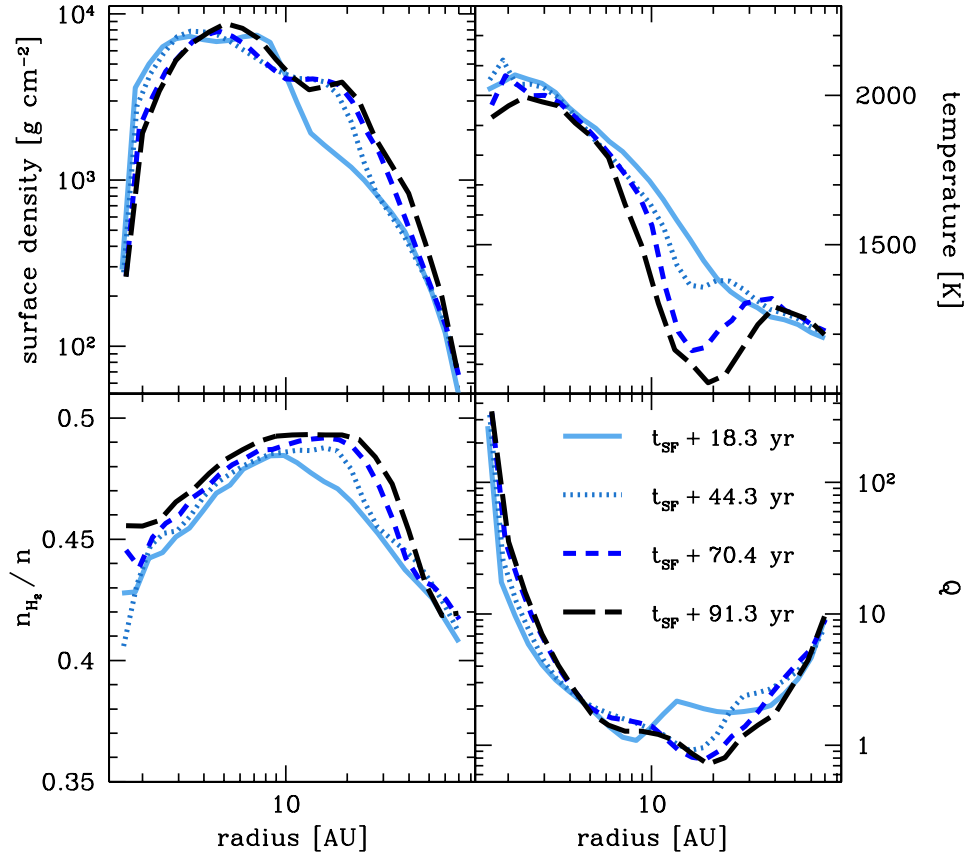


Figure 2: Radial profiles of the disk’s physical properties, centered on the first protostellar core to form. The quantities are mass-weighted and taken from a slice through the midplane of the disk. In the lower right-hand plot we show the radial distribution of the disk’s Toomre parameter, $Q = c_s \kappa / \pi G \Sigma$, where c_s is the sound speed and κ is the epicyclic frequency. Because our disk is Keplerian, we adopted the standard simplification, and replaced κ with the orbital frequency. The molecular fraction is defined as the number density of hydrogen molecules (n_{H_2}), divided by the number density of hydrogen nuclei (n), such that fully molecular gas has a value of 0.5

gravitating disks, in which gravitational torque provides the main source of angular momentum transport. Although the spiral pattern started out fairly symmetric, it quickly developed non-axisymmetric features. Eventually, the gas in one of the spiral arms became locally unstable and started to collapse, forming a second protostar at a distance of roughly 20 AU from the primary. The mass of the central protostar at this point was only $0.5 M_{\odot}$.

The surface density remained roughly constant as the disk grew, with the temperature behaving in a similar fashion and thus the ability of the disk to transport angular momentum remained the same as the disk grew. This can be seen by considering the Toomre ‘ Q ’ parameter (Fig. 2), which provides a measure of the gravitational instability of the disk. For high Q , the disk is stable, while for values around 1, the disk is formally unstable to fragmentation. As the disk grew, the value of Q remained around 1 in the outer regions, and so the dynamics of the disk were dominated by gravitational instabilities.

Figure 3, which shows the accretion rate through the disk and envelope as a function of radius from the central protostar, helps to explain why the disk became so unstable. The accretion rate through the disk was considerably lower than the rate at which material was added to the disk. If one assumes a simple α -disk model (12), then the disk accreted with an effective α between 0.1 and 1, which is typical for gravitational torques in strongly self-gravitating disks (S26). Although this is an efficient mechanism for transporting angular momentum, it was nevertheless unable to process the material in the disk quickly enough before more was added from the infalling envelope. As a result, the disk grew in mass, became gravitationally unstable, and ultimately fragmented.

For a region of the disk to form a new star, it must be able to rid itself of the heat generated as it collapses, and further, it must do so before the motions in the disk shear the region apart (S34). In the case of a primordial protostellar disk, this cooling is provided by molecular hydrogen. At typical disk number densities, around 10^{12} to 10^{14} cm^{-3} , most of the cooling

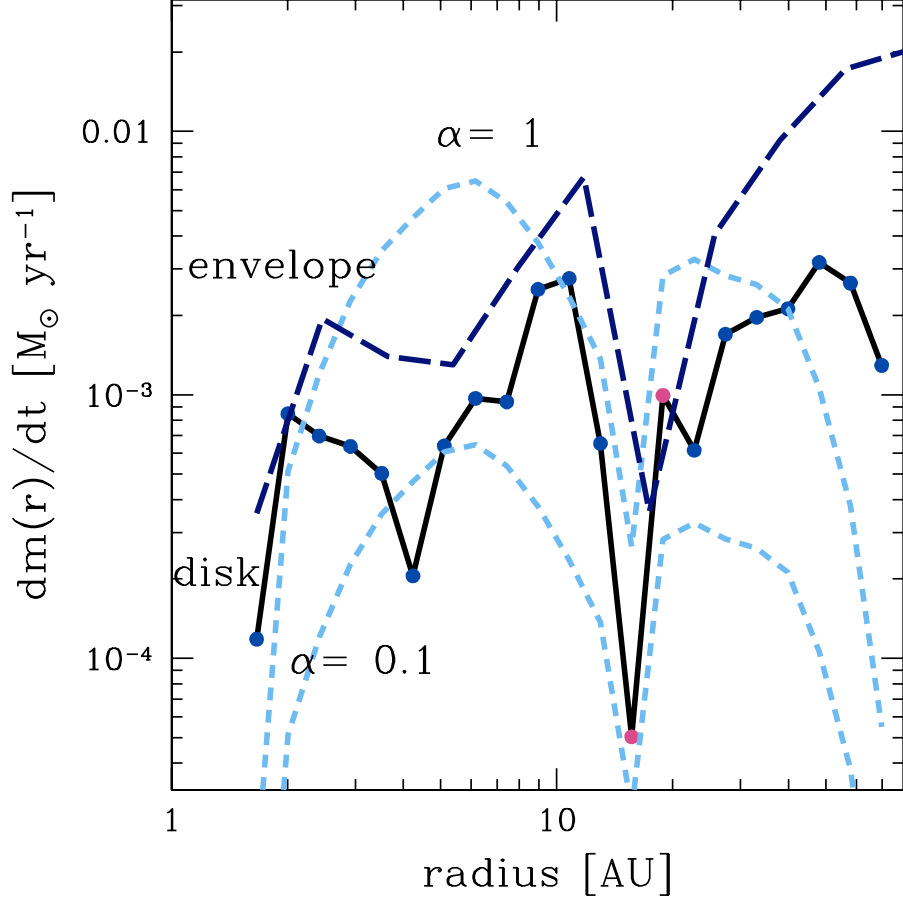


Figure 3: The mass transfer rate through the disk is denoted by the solid black line, while the mass infall rate through spherical shells with the specified radius is shown by the dark blue dashed line. The latter represents the total amount of material flowing through a given radius, and is thus a measure of the material flowing through *and onto* the disk at each radius. Both are shown at the onset of disk fragmentation. In the case of the disk accretion we have denoted annuli that are moving towards the protostar with blue dots, and those moving away in pink (further details can be found in Section 6 of the online material). The light blue dashed lines show the accretion rates expected from an ‘alpha’ (thin) disk model, where $\dot{M}(r) = 3\pi\alpha c_s(r)\Sigma(r)H(r)$, with two global values of alpha and where $c_s(r)$, $\Sigma(r)$, and $H(r)$ are (respectively) the sound speed, surface density and disk thickness at radius r .

comes from H₂ line emission. In the centers of the spiral arms, or at number densities of around 10¹⁴ cm⁻³, cooling by collision-induced emission (CIE) from H₂ begins to dominate, and it is this process that allowed the initial gravitational fragmentation to take place in the spiral arms (see Section 6 of 10). At number densities of around 10¹⁶ cm⁻³, the gas becomes optically thick to CIE, and begins to heat up further as it is compressed. However, it turns out that primordial protostellar accretion disks are unusual in that the dissociation of molecular hydrogen plays an important role in regulating their temperature evolution. In contrast to present-day star formation, primordial protostellar disks are remarkably hot (Fig. 2). Any further compression causes the hydrogen molecules to dissociate, removing energy from the system. This process acts like a thermostat, keeping the temperature in the collapsing region roughly constant while the collapse proceeds. Thus, perhaps somewhat counter-intuitively, it is the relatively high temperature associated with primordial star formation, coupled with a high molecular fraction, that allowed the protostellar accretion disk to fragment.

Fragmentation does not stop with the formation of a second protostar. Only four years after the initial fragmentation of the disk, the dense ridge in a neighboring spiral arm also fragmented, forming a third protostar. Fifteen years later, the disk fragmented yet again and the protostars evolved into a chaotic multiple system. At the stage of the evolution shown in Fig. 1, slightly less than 1 M_⊙ of gas had been converted into protostars, and hence the system was still very much in its infancy. Eventually, beyond the epoch followed by our current calculation, the disk will lose its ability to fragment once the heating from the protostars becomes strong enough to dissociate all of the H₂, thereby removing the major coolant (15). However the system will continue to accrete infalling gas from the collapsing envelope, until one of the protostars becomes sufficiently hot to ionize the gas, which finally terminates the accretion (7).

Are our results representative of primordial star formation in general, or is the gas within our halo special in some way? The properties of the gas that assembled the disk in our simulation

were remarkably similar to those found in other simulations of primordial star formation (10). Crucially, the angular momentum of the inner $4 M_{\odot}$ – the combined mass of the disk and the protostar at the point of fragmentation – was $1.4 \times 10^{-3} \text{ km s}^{-1} \text{ pc}$, comparable to the $1.2 \times 10^{-3} \text{ km s}^{-1} \text{ pc}$ reported elsewhere (1). Fragmentation of the kind we have seen should therefore be a normal part of the formation of primordial stars, suggesting that the endpoint of the Pop III star formation process is significantly more complicated than previously thought. Idealized calculations have previously found hints of such widespread binarity among the first stars (16), but our work establishes this property for realistic cosmological initial conditions, coupled with the radiative feedback, and the extremely high resolution needed to address protostellar disk evolution.

While our simulations do not show how primordial disks evolve beyond the initial disk fragmentation, present-day star formation calculations (11, 17, 18) predict that as fragmentation proceeds in high-mass accretion disks, new protostars form at increasingly larger radii. Because gas can only be accreted when its angular momentum matches that of the protostar, it is easier for the new objects than for the preexisting ones to gain fresh gas that moves inwards through the accretion disk, tending to drive the system towards equal masses (19). If fragmenting Pop III systems evolved in a similar fashion, then one plausible outcome of primordial star formation would be the formation of nearly equal-mass Pop III binaries. Their potential existence would strengthen the case for high-redshift gamma-ray bursts origination from the first stars (20). From present-day star formation, we also know that young multiple systems are dynamically unstable, over time leading to the dynamical ejection of protostars (21) with the preferentially close, high-mass binary systems remaining in the center. If Pop III stars were dynamically ejected from such systems before accreting very much gas, then there is the possibility that some of these stars may have had masses low enough for them to have survived until the present-day.

References

1. T. Abel, G. L. Bryan, M. L. Norman, *Science* **295**, 93 (2002).
2. V. Bromm, P. S. Coppi, R. B. Larson, *Astrophys. J.* **564**, 23 (2002).
3. B. W. O'Shea, M. L. Norman, *Astrophys. J.* **654**, 66 (2007).
4. N. Yoshida, K. Omukai, L. Hernquist, T. Abel, *Astrophys. J.* **652**, 6 (2006).
5. N. Yoshida, K. Omukai, L. Hernquist, *Science* **321**, 669 (2008).
6. V. Bromm, A. Loeb, *New Astronomy* **9**, 353 (2004).
7. C. F. McKee, J. C. Tan, *Astrophys. J.* **681**, 771 (2008).
8. M. J. Turk, T. Abel, B. O'Shea, *Science* **325**, 601 (2009).
9. A. Stacy, T. H. Greif, V. Bromm, *Mon. Not. R. Astron. Soc.* **403**, 45 (2010).
10. Materials and methods are available as supporting material on Science Online.
11. M. R. Krumholz, R. I. Klein, C. F. McKee, S. S. R. Offner, A. J. Cunningham, *Science* **323**, 754 (2009).
12. N. I. Shakura, R. A. Sunyaev, *A & A* **24**, 337 (1973).
13. G. Lodato, W. K. M. Rice, *Mon. Not. R. Astron. Soc.* **358**, 1489 (2005).
14. C. F. Gammie, *Astrophys. J.* **553**, 174 (2001).
15. J. C. Tan, C. F. McKee, *Astrophys. J.* **603**, 383 (2004).
16. M. N. Machida, K. Omukai, T. Matsumoto, S. Inutsuka, *Astrophys. J.* **677**, 813 (2008).

17. T. Peters, *et al.*, *Astrophys. J.* **711**, 1017 (2010).
18. T. Peters, R. S. Klessen, M. Mac Low, R. Banerjee, *Astrophys. J.* **725**, 134 (2010).
19. M. R. Bate, I. A. Bonnell, *Mon. Not. R. Astron. Soc.* **285**, 33 (1997).
20. V. Bromm, A. Loeb, *Astrophys. J.* **642**, 382 (2006).
21. S. Portegies Zwart, S. McMillan, M. Gieles, *ArXiv e-prints* **1002.1961** (2010).
22. We acknowledge financial support from: the *Baden-Württemberg Stiftung* via their program International Collaboration II (grant P-LS-SPII/18); a Frontier grant of Heidelberg University sponsored by the German Excellence Initiative; NSF grants AST-0708795 and AST-1009928; and NASA through Astrophysics Theory and Fundamental Physics Program grants NNX 08-AL43G and 09-AJ33G (V.B.). This research used the Ranger system at the Texas Advanced Computing Center (TeraGrid award AST090003).

Supporting Online Material for The Formation and Fragmentation of Disks around Primordial Protostars

Paul C. Clark,* Simon C. O. Glover, Rowan J. Smith, Thomas H. Greif, Ralf S.
Klessen, Volker Bromm

*To whom correspondence should be addressed; E-mail: pcc@ita.uni-heidelberg.de

1 Numerical methods

The simulations discussed in this paper were performed using a modified version of the Gadget 2 smoothed particle hydrodynamics (SPH) code (*S1*). Our modifications involve the addition of a treatment of primordial chemistry and cooling, along with a scheme for replacing gas in unresolved regions with collisionless “sink” particles (*S2, S3*). We have also implemented an approximate model for the effects of the accretion luminosity produced by the accreting protostars. Details of these modifications are given below.

Chemistry and cooling To model the chemical evolution of the metal-free gas, we use a chemical network consisting of 45 reactions amongst twelve chemical species: H, H⁺, H⁻, H₂⁺, H₂, He, He⁺, He⁺⁺, D, D⁺, HD, and free electrons (*S4*). For most of these reactions, we use the same reaction rate coefficients as in Clark et al. (*S4*). The exceptions are the three-body reaction



and its inverse reaction, the collisional dissociation of H₂ by H,



Considerable uncertainty exists concerning the rate of reaction 1 at low temperatures (*S6*). We adopt the rate coefficient given for this reaction by Abel et al. (*S5*), which is the smallest of those in common usage, and hence will yield the highest temperature for the dense gas in the center of the minihalo (*S7*). This warmer gas is less likely to fragment than the cooler gas yielded by alternative choices for the three-body reaction rate coefficient. Moreover, accretion disks formed in simulations run with a small value for the three-body rate coefficient are less likely to be H₂-dominated than those formed in simulations using a larger value for the rate coefficient, and so again will be more stable against fragmentation. In view of this, we consider our choice

of the Abel et al. rate coefficient to be conservative, in the sense that it will tend to reduce the likelihood of fragmentation.

Our decision to use a different rate coefficient for Reaction 1 than in the Clark et al. study means that we must also adopt a different rate coefficient for reaction 2, as at high densities the ratio between the rate coefficients of reactions 1 and 2 must satisfy

$$\frac{k_1}{k_2} = K, \quad (3)$$

where k_1 and k_2 are the rate coefficients for reactions 1 and 2, respectively, and where K is the equilibrium constant for the pair of reactions, given by (S8)

$$K = 1.05 \times 10^{-22} T^{-0.515} \exp\left(\frac{52000}{T}\right). \quad (4)$$

Note that the value of K does not depend on our choice of values for k_1 or k_2 , and hence we cannot vary these rate coefficients independently: if we change k_1 , we must also adjust k_2 such that Equation 4 remains satisfied.

Our treatment of the cooling also follows the Clark et al. study. We account for the full set of processes described in that paper, including electronic excitation of H, He and He⁺, cooling from the recombination of H⁺ and He⁺, Compton cooling and bremsstrahlung. However, in practice only a few processes play an important role at the densities and temperatures characteristic of the protostellar accretion disk – H₂ rotational and vibrational line cooling, H₂ collision-induced emission (CIE) cooling, H₂ collisional dissociation cooling, and heating due to three-body H₂ formation.

We model H₂ line cooling in the optically thin regime using a comprehensive treatment that includes the effects of collisions between H₂ molecules and H and He atoms, other H₂ molecules, protons and electrons (S9), and that accounts for the transition to local thermodynamic equilibrium level populations at number densities $n \gg 10^4 \text{ cm}^{-3}$. At densities $n \sim$

10^9 cm^{-3} and above, the strongest of the H_2 ro-vibrational lines become optically thick, reducing the effectiveness of H_2 line cooling. To account for this effect, we use an approach based on the Sobolev approximation (*SIO*). We write the H_2 cooling rate as

$$\Lambda_{\text{H}_2} = \sum_{u,l} \Delta E_{ul} A_{ul} \beta_{\text{esc},ul} n_u, \quad (5)$$

where n_u is the number density of hydrogen molecules in upper energy level u , ΔE_{ul} is the energy difference between this upper level and a lower level l , A_{ul} is the spontaneous radiative transition rate for transitions between u and l , and $\beta_{\text{esc},ul}$ is the escape probability associated with this transition, i.e. the probability that the emitted photon can escape from the region of interest. We fix n_u by assuming that the H_2 level populations are in local thermodynamic equilibrium, and write the escape probabilities for the various transitions as (*SIO*)

$$\beta_{\text{esc},ul} = \frac{1 - \exp(-\tau_{ul})}{\tau_{ul}}, \quad (6)$$

where we use the approximation that

$$\tau_{ul} \simeq \alpha_{ul} L_s \quad (7)$$

where α_{ul} is the line absorption coefficient and L_s is the Sobolev length. In the classical, one-dimensional spherically symmetric case, the Sobolev length is given by

$$L_s = \frac{v_{\text{th}}}{|dv_r/dr|}, \quad (8)$$

where v_{th} is the thermal velocity, and dv_r/dr is the radial velocity gradient. In our three-dimensional simulations, we generalize this as (*SII*)

$$L_s = \frac{v_{\text{th}}}{|\nabla \cdot \mathbf{v}|}, \quad (9)$$

To prevent the H_2 cooling rate from being reduced by an unphysically large amount in regions with small velocity gradients, we limit L_s to be less than or equal to the local Jeans length, L_J .

We justify this choice of limit by noting that there are strong density gradients in the gas on scales $L \gg L_J$, and so we expect the bulk of the contribution to the H₂ line absorption to come from material within only a few Jeans lengths.

At very high densities ($n > 10^{14} \text{ cm}^{-3}$), CIE cooling from H₂ becomes more effective than H₂ line cooling (S12). We model this as discussed in Clark et al., and account for the reduction of the CIE cooling rate due to the effects of continuum opacity using the following empirical prescription, based on previous high-resolution 1D calculations of the formation of primordial protostars (S12, S13)

$$\Lambda_{\text{CIE,thick}} = \Lambda_{\text{CIE,thin}} \min \left(\frac{1 - e^{-\tau_{\text{CIE}}}}{\tau_{\text{CIE}}}, 1 \right), \quad (10)$$

where

$$\tau_{\text{CIE}} = \left(\frac{n_{\text{H}_2}}{7 \times 10^{15} \text{ cm}^{-3}} \right)^{2.8}. \quad (11)$$

The reduction in the CIE cooling rate predicted by this prescription agrees to within a factor of a few with that measured in a more recent 3D simulation of Pop. III star formation (S14), but this simulation followed the evolution of the gas only prior to the formation of the initial protostar, and hence could not test the validity of the empirical prescription at later times in the evolution of the system. In particular, it is unclear whether Eq. 11 remains a good approximation once material begins to build up in the protostellar accretion disk. To test this, we selected a set of SPH particles covering a range of different number densities in the output snapshot produced immediately prior to the formation of the second sink particle. We computed continuum opacities along forty-eight different lines of sight surrounding each SPH particle by solving the equation

$$\tau_i = \int_0^{L_i} \rho(l) \kappa_{\text{P}}(\rho, T, x_{\text{H}_2}) dl \quad (12)$$

along each line of sight, where L_i is the distance from the particle to the edge of the simulation volume, $\rho(l)$ is the local density at a distance l along the line of sight, T is the temperature at

the same point, $x_{\text{H}_2} = n_{\text{H}_2}/n$, and κ_{P} is the Planck mean opacity of the gas. The mean opacity is a function of the local density, temperature and chemical composition, and we calculated it by interpolation from previously tabulated values (S15). An estimate of τ_{CIE} then follows from

$$\exp(-\tau_{\text{CIE}}) = \frac{1}{48} \sum_{i=1}^{48} \exp(-\tau_i). \quad (13)$$

We then used Eq. 10 together with this estimate of the CIE opacity to compute the reduction in the CIE cooling rate, and compared this with the reduction predicted by our empirical prescription. The results are plotted in Figure S4. We see that in practice, the continuum opacity begins to reduce the CIE cooling rate somewhat earlier than would be predicted by Eqs. 10–11, but that at densities above $n \sim 10^{16} \text{ cm}^{-3}$, the two different techniques yield very similar answers. Moreover, the difference between the reduction factor (i.e. the ratio of the optically thick and optically thin CIE cooling rates) predicted by Eqs. 10–11 and the one computed from our simulation results is never greater than a factor of two over the whole of the regime where CIE cooling is important. Given the very strong temperature dependence of the CIE cooling ($\Lambda_{\text{CIE}} \propto T^4$), a factor of two uncertainty in the cooling rate translates into only a 20% uncertainty in the gas temperature, which is unlikely to be large enough to significantly affect the conclusions of our study. Furthermore, it should also be noted that gas at the typical densities of $n \sim 10^{13}\text{--}10^{15} \text{ cm}^{-3}$ found in the accretion disk remains in the optically thin regime as far as CIE cooling is concerned. The effects of continuum opacity only become important in gas that is already undergoing run-away gravitational collapse.

Finally, our thermal model also accounts for changes in the internal energy of the gas due to the dissociation or formation of H_2 molecules. Every collisional dissociation of an H_2 molecule requires 4.48 eV of energy (the binding energy of the H_2 molecule), which is removed from the thermal energy of the gas, while every time that a new H_2 molecule is formed by the three-body process, the gas gains 4.48 eV of thermal energy. For a gas in chemical equilibrium, the

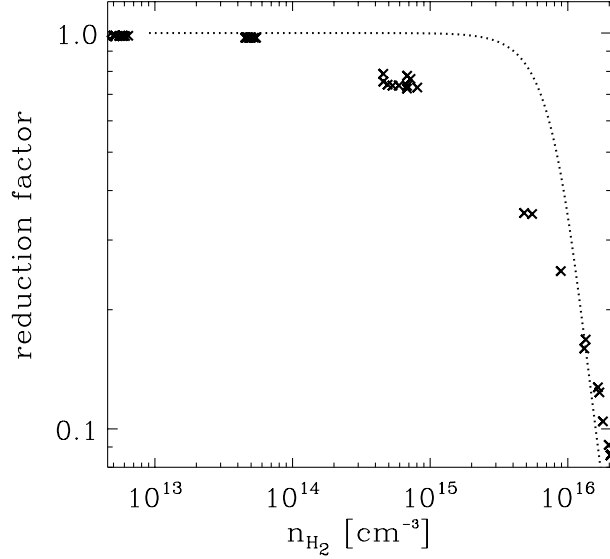


Figure 4: The ratio $\Lambda_{\text{CIE,thick}}/\Lambda_{\text{CIE,thin}}$, plotted as a function of the number density of H_2 . The solid line gives the values predicted by our empirical prescription (Eqs. 10–11), while the individual data points show the results of the more sophisticated procedure described in the text.

simplest way to account for these effects is through the equation of state of the gas. Given the hydrogen nuclei number density n and the gas temperature T , the equilibrium molecular fraction $x_{\text{H}_2} = n_{\text{H}_2}/n$ can be determined from the Saha equation, and the specific internal energy u can then be obtained by summing up the contributions due to the translational motions of the hydrogen molecules, hydrogen atoms and helium atoms, the internal degrees of freedom of the hydrogen molecules, and the dissociation energy of the H_2 molecules (S16). A convenient way to visualize how u varies with temperature is to examine the behaviour of the specific heat capacity, u/RT , where $R = k_{\text{B}}/m_{\text{H}}$, k_{B} is Boltzmann’s constant, and m_{H} is the mass of a hydrogen atom. In Figure S5, we show how u/RT varies with temperature for several different values of n . At low temperatures, the specific heat capacity is almost independent of temperature, but above a temperature of 1500–2000 K, it rises sharply as the H_2 begins to dissociate. Physically, this means that once the gas reaches this temperature regime, a much

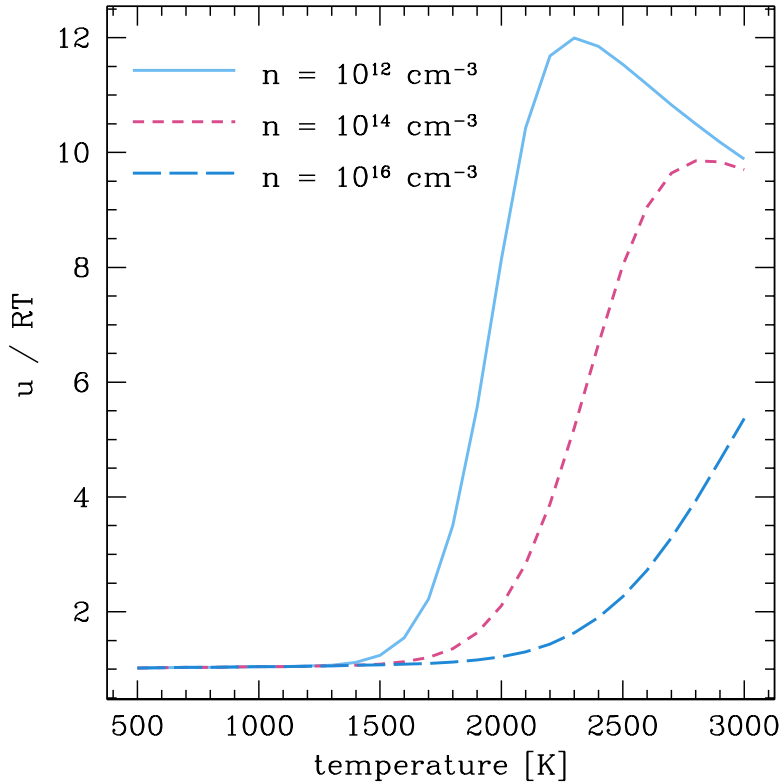


Figure 5: The specific heat capacity u/RT of primordial gas (where u is the specific energy and $R = k_B/m_H$), computed assuming chemical equilibrium, and plotted as a function of temperature for three different values of the hydrogen nuclei number density n . At low temperatures, the specific heat capacity is almost independent of T , but it increases sharply above $T \sim 1500$ – 2000 K as the H_2 in the gas begins to dissociate.

greater amount of energy is required in order to raise the temperature further than would be the case in colder gas. We see this effect in our simulations, in the gas undergoing run-away gravitational collapse in the disk: despite being strongly heated by compression, it increases its temperature only slowly once it reaches the temperature regime in which H_2 dissociation begins to occur.

Unfortunately, although this approach is useful for providing insight into the thermodynamical behaviour of the gas, it relies on the gas being in chemical equilibrium, which is not the

case for the majority of the gas in our simulations. Chemical equilibrium is reached only for gas number densities above $n \sim 10^{15} \text{ cm}^{-3}$ (S14). Therefore, rather than account for H₂ formation heating and dissociation cooling by including their effects in our adopted equation of state, we instead follow previous studies (S10, S14) and include a chemical heating/cooling term $\dot{e}_{\text{chem}} = \chi_{\text{H}_2} \dot{n}_{\text{H}_2}$ in our equation for the time evolution of the internal energy density of the gas, where $\chi_{\text{H}_2} = 4.48 \text{ eV}$ and \dot{n}_{H_2} is the rate of change of the H₂ number density, computed with the mass density ρ held constant.

Sink particles We create sink particles following the standard SPH prescription (S2), and adopt a threshold density for sink particle creation $n_{\text{th}} = 10^{17} \text{ cm}^{-3}$. At this density, radiative cooling of the gas has become almost completely ineffective, and the dominant cooling process is collisional dissociation of H₂ (see Section 7 below). We therefore do not expect significant fragmentation of the gas to occur at densities $n > n_{\text{th}}$. Any SPH particle that exceeds our threshold density is potentially eligible to be converted into a sink particle, but sink particle creation occurs only for particles satisfying several additional criteria. First, the candidate sink particle must be located a distance $r \geq 2r_{\text{acc}}$ away from any other sink particle, where r_{acc} is the sink particle accretion radius (see below). This criterion prevents sink particle formation from occurring within gas that is about to be accreted by another sink particle. Second, we check to see whether the smoothing length of the particle is less than the accretion radius of the sink particle that it will become. This test ensures that we are resolving the structure of the gas within the sink particle accretion radius. Third, we ensure that the candidate sink particle and its nearest neighbors are all on the same integration time-step. Once these preliminary criteria are met, the dynamical state of the candidate sink particle and its neighbors is examined. In order to ensure that sink particle creation occurs only within gas which is undergoing gravitational collapse, we require that the total energy of the candidate sink plus the gas within one smoothing

length be negative, implying that the collection of SPH particles are gravitationally bound, and also verify that the divergence of the particle accelerations is negative. This final check ensures that the group of particles is not in the process of being tidally disrupted or bouncing. If all of these tests are passed, the candidate particle is converted into a sink particle. Its fifty nearest neighbors are removed from the simulation, and their masses and linear momenta are added to the sink particle.

As the simulation progresses, sink particles are allowed to accrete other gas particles that move to within $r < r_{acc}$ of the sink particle. However, gas particles within the accretion radius are accreted only if they pass several additional tests. First, they must be gravitationally bound to the sink particle, and moving towards it. Second, if more than one sink is present, they must be bound more strongly to the candidate sink than to any other sink in the simulation. Third, the gas particle and the sink must be on the same integration time-step. Once these tests are passed, the mass and linear momentum of the SPH particle are added to the sink particle, and the SPH particle is removed from the simulation.

In the simulations presented in this paper, we set $r_{acc} = 1.5$ AU. Gravitational forces are softened on a significantly smaller length scale of 0.066 AU to ensure that the force exerted by the sink particle on gas outside of the accretion radius is essentially the same as that of a point mass, and to permit sinks to come close enough together to allow us to check for potential mergers. For comparison, the minimum SPH smoothing length resolvable in the simulation is 0.0551 AU, and so we resolve pressure gradients on a similar scale to gravitational forces, as is required to prevent artificial fragmentation (*S17*). We check for mergers between sinks by examining whether any two sinks ever come within two protostellar radii of each other, taking $50 R_{\odot}$ as a reasonable estimate for the pre-main sequence radii of the Population III stars studied in this simulation (see Eq. 15 below). In this study, we find no evidence for any potential mergers.

We have also performed a simulation with a larger sink accretion radius of 3 AU. The gravitational softening length in this simulation was again fixed at 0.066 AU. This simulation produced qualitatively similar results to those from an $r_{\text{acc}} = 1.5$ AU simulation with the same assumed protostellar accretion rate. In the simulation with the larger accretion radius, the first signs of fragmentation appeared at a distance of 8 AU from the central protostar, roughly twice the separation seen in the simulation with $r_{\text{acc}} = 1.5$ AU. As in the simulations with smaller r_{acc} , the disk proceeded to fragment further. The difference between the two simulations is easily explained. When the sink particles have smaller accretion radii, we are able to resolve fragmentation that occurs on smaller scales. In this particular case, the simulation performed using an accretion radius of 1.5 AU was able to model the formation of an object that was swallowed by the sink particle in the simulation performed with the 3 AU accretion radius. The third object to form in the $r_{\text{acc}} = 1.5$ AU simulation is located in roughly the same place as the second object in the $r_{\text{acc}} = 3$ AU simulation, demonstrating that the evolution of the disk at distances $r \gg r_{\text{acc}}$ is largely unaffected by the choice of r_{acc} .

Accretion luminosity We treat each sink particle formed in our simulation as a separate protostar, and account for the energy released by accretion onto the surfaces of these protostars. To model the effects of this accretion luminosity, we first compute the bolometric accretion luminosity for each accreting protostar

$$L_{\text{acc}} = \frac{G\dot{M}_*M_*}{R_*}, \quad (14)$$

where \dot{M}_* is the accretion rate onto the protostar, M_* is the protostellar mass and R_* is the protostellar radius. In this study, we model only the first few hundred years of evolution of the protostellar system. Since the Kelvin-Helmholtz relaxation timescale of even a high-mass protostar is of the order of a few thousand years (*S18*), we can be confident that the protostars in our simulation will not yet have thermally relaxed, and will still be in the initial adiabatic

accretion phase. We therefore relate the protostellar radius to the current protostellar mass and mass accretion rate using the following relationship (S19)

$$R_* = 26R_\odot \left(\frac{M_*}{M_\odot} \right)^{0.27} \left(\frac{\dot{M}_*}{10^{-3} M_\odot \text{ yr}^{-1}} \right)^{0.41}, \quad (15)$$

which was derived for adiabatically accreting, metal-free protostars embedded in a spherically symmetric inflow. More recent calculations for the case of rotating infall (S20) find an even larger value for R_* during the adiabatic accretion phase (see their Fig. 5), and so using the expression given by Equation 15 provides us with a conservative upper limit on the bolometric accretion luminosity during this phase.

Combining Eqs. 14 and 15, we find that

$$L_{\text{acc}} \simeq 1200L_\odot \left(\frac{M_*}{M_\odot} \right)^{0.73} \left(\frac{\dot{M}_*}{10^{-3} M_\odot \text{ yr}^{-1}} \right)^{0.59}. \quad (16)$$

Using this expression for the bolometric accretion luminosity, we next determine the heating rate of the gas surrounding the protostar from

$$\Gamma_* = \rho \kappa_{\text{P}} \frac{L_{\text{acc}}}{4\pi r^2}, \quad (17)$$

where ρ is the mass density, r is the distance to the protostar, and κ_{P} is the Planck mean opacity of the gas. We calculate this mean opacity by interpolation, using tabulated values that include the effects of both line and continuum absorption, and that account for the extra electrons provided by ionized lithium (S15). Equation 17 assumes that the gas is optically thin to the radiation from the accreting protostar. In reality, this is unlikely to be the case. However, making this assumption allows us to avoid the extremely high computational cost that would be associated with an accurate treatment of the transfer of the protostellar radiation, and also gives us a conservative upper limit on the effectiveness of the protostellar feedback.

To determine L_{acc} , and hence Γ_* , we need to know the accretion rate onto the protostar, \dot{M}_* . Determining this self-consistently during the simulation is difficult, owing to the particle-based

nature of our hydrodynamical model. The smallest amount of gas that can be accreted during any given hydrodynamical time-step is that corresponding to a single SPH particle, i.e. $10^{-5}M_{\odot}$, and hence accretion onto the sink particle proceeds as a series of discrete increments, rather than a smooth increase in the sink particle mass. To obtain an accurate value for the accretion rate, we therefore need to average over a large enough number of time-steps to wash out this artificial discreteness. In the simulation discussed in the main paper, we achieve this by recording the mass accreted by the sink particle during each hydrodynamical time-step, and determine the current value of \dot{M}_* by computing a smoothed average of the accretion rate over the previous ten years. For times less than ten years after the formation of the protostar, we average over a shorter period, and take the instantaneous accretion rate at the time that the sink particle forms to be $\dot{M}_* = 5 \times 10^{-2} M_{\odot} \text{ yr}^{-1}$, an overestimate of the true value (see Figure S6). As the protostellar accretion rate typically decreases over time, this procedure gives us a slight overestimate of the true rate, as can be seen in Figure S6, where we compare our estimated accretion rate (denoted by the black line) with the actual accretion rate onto the protostar (magenta line), which we measure during a post-processing step. In order to explore the sensitivity of our results to our method for determining \dot{M}_* , we have also performed two simulations in which the accretion rate used within our accretion luminosity calculation is not determined self-consistently during the simulation, but is instead maintained at a fixed value throughout. In these two simulations, we set $\dot{M}_* = 10^{-3} M_{\odot} \text{ yr}^{-1}$ and $\dot{M}_* = 10^{-2} M_{\odot} \text{ yr}^{-1}$, respectively, as these values bracket the true value of \dot{M}_* during almost all of the period of time simulated, as illustrated in Figure S7. These simulations produce qualitatively and quantitatively similar results to our primary simulation, as demonstrated in Section 4 below.

Finally, we note that in our current simulations, we do not account for the photodissociation of H_2 molecules in the surrounding gas by radiation from the central protostar. We justify this omission by noting that during the adiabatic accretion phase, the protostar has a very large radius

(see Eq. 15 above), and hence a low effective temperature. Therefore, only a very small fraction of the bolometric accretion luminosity of the protostar is emitted in the form of ultraviolet photons energetic enough to photodissociate H_2 . As an illustrative example, consider the case of an $0.5M_\odot$ protostar accreting at a rate $\dot{M}_* = 10^{-3}M_\odot \text{ yr}^{-1}$: from Eqs. 15–16 above, we find that the radius and luminosity of the protostar would be roughly $20 R_\odot$ and $720 L_\odot$, respectively, from which it follows that the effective temperature of the protostar at this point is roughly 6500 K (where we have approximated the protostellar emission as being from a pure black-body). The fraction of the protostellar luminosity that falls within the Lyman-Werner bands of H_2 is therefore roughly 10^{-8} , and so the accreting protostar emits roughly 10^{39} photons s^{-1} within the Lyman-Werner bands. Even if we assume that every single one of these photons is absorbed and causes the dissociation of an H_2 molecule, the rate at which H_2 is destroyed by photodissociation is less than $10^{-10} M_\odot \text{ yr}^{-1}$, and hence only a negligible amount of H_2 would be destroyed during the period covered by our simulations.

2 Initial conditions

We begin our study with a cosmological simulation. We model the evolution of dark matter in a box with a side length of 200 comoving kpc. The cosmological simulation is initialized at $z = 99$ with a standard ΛCDM fluctuation power spectrum, with a matter density $\Omega_m = 1 - \Omega_\Lambda = 0.3$, baryon density $\Omega_b = 0.04$, Hubble parameter $h = H_0/100 \text{ km s}^{-1} \text{ Mpc}^{-1} = 0.7$, spectral index $n_s = 1.0$ and normalization $\sigma_8 = 0.9$ (S21). Following the zoom technique used in Greif et al. (S22), we first run a coarse dark matter (DM) simulation with 128^3 particles and a particle mass of $\simeq 150 M_\odot$ until the first minihalo exceeding a mass of $5 \times 10^5 M_\odot$ collapses. We then reinitialize the simulation at $z = 99$ with additional small-scale power in a cube with 50 kpc (comoving) on a side, centered on the location of the minihalo formed in the previous step, and replace each DM particle in the original simulation with 512 DM and 512 gas

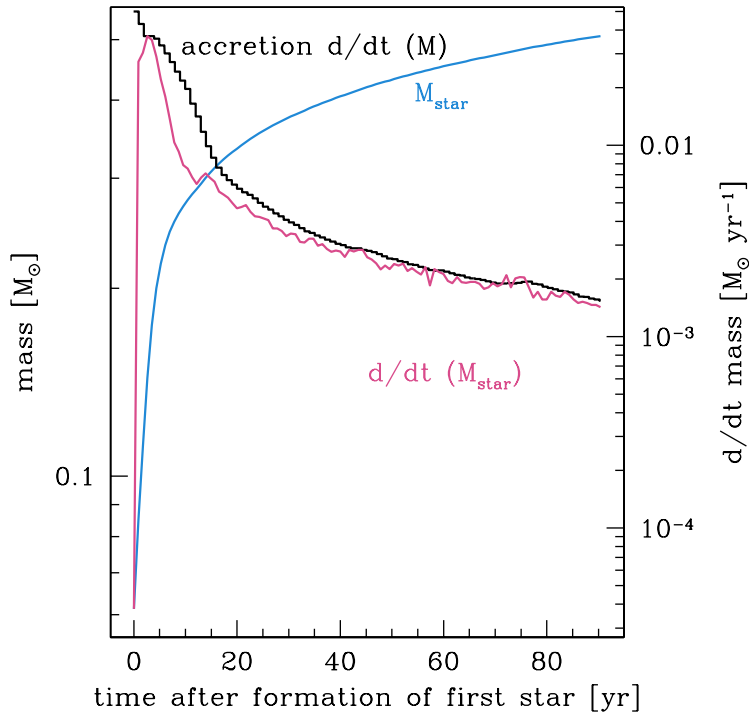


Figure 6: Evolution with time of the mass of the first sink particle (*blue curve*), the true accretion rate onto the protostar (*magenta curve*) and the time-averaged estimate of the accretion rate used to computing the accretion luminosity (*black curve*). Our estimate is a slight overestimate of the true accretion rate, particularly at early times when the accretion rate is changing rapidly with time.

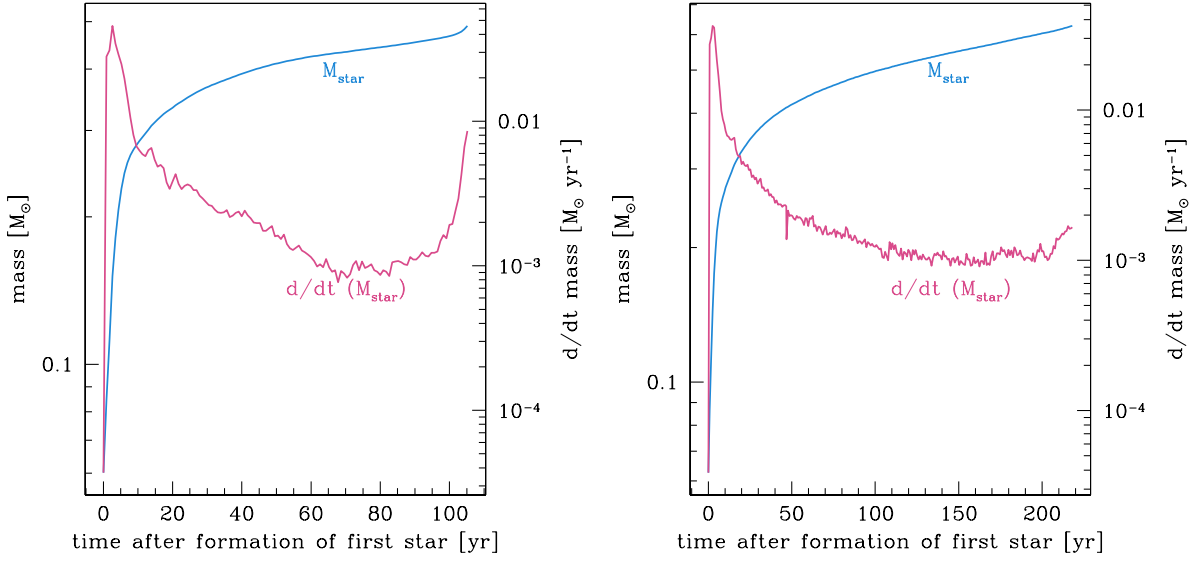


Figure 7: *Left panel:* Evolution with time of the mass of the first sink particle (*blue curve*) and the accretion rate onto that sink particle (*magenta curve*) in the simulation in which we assume an accretion rate of $10^{-3} M_{\odot} \text{ yr}^{-1}$ for the purposes of computing the accretion luminosity. The true accretion rate remains a factor of a few larger than this assumed rate throughout most of the simulation. The rise in the accretion rate visible at $t \sim 100 \text{ yr}$ is a consequence of the same gravitational instability that leads to the formation of the second sink particle. The local contraction of the spiral arm causes material to be pulled back in its orbit, towards the collapsing region, where it collides with other material. This process causes a sufficient loss of angular momentum that the orbit can no longer be maintained and the gas moves inwards, resulting in an increased accretion rate onto the central protostar. *Right panel:* Evolution with time of the sink-mass and accretion rate in the simulation in which we assume an accretion rate of $10^{-2} M_{\odot} \text{ yr}^{-1}$. In this simulation, the true accretion rate onto the sink remains smaller than the assumed value throughout most of the simulation. It exceeds the assumed value only at very early times after the formation of the first sink, although we caution that the numerical resolution of this initial burst of accretion is poor, and that we may be overestimating the rate at which it occurs. In this simulation, we also see a rise in the accretion rate associated with the formation of the second sink particle, but the magnitude of the increase is much smaller. This is a consequence of the fact that the spiral structure close to the protostar is much less pronounced, owing to the greater amount of heating produced by the increased accretion luminosity.

particles. Outside of this region, a sufficiently large buffer zone is created, where the particle mass increases in factors of eight until the mass resolution of the original DM simulation is obtained. The final DM and gas particle masses in the high resolution region are $\simeq 0.3$ and $0.04 M_{\odot}$, respectively. We then re-run the cosmological simulation, evolving the gas and dark matter until the gas in the minihalo has reached a number density of 10^6 cm^{-3} , by which point the gas has gravitationally decoupled from its parent minihalo and has begun to collapse in its own right. This occurs at a redshift $z \sim 17$, at which time the virial mass of the dark matter halo is $3.3 \times 10^5 M_{\odot}$. Note that this value is smaller than the mass quoted above because the runaway collapse of the gas cloud occurs slightly earlier than the time at which the minihalo was identified in the DM-only simulation.

At this point we discard the full cosmological simulation and focus our calculation on the central collapsing region and its immediate surroundings. These then become the initial conditions for the second phase of our study. The initial gravitational instability that leads to the collapse in the baryons occurs at a number density of around $n \sim 10^4 \text{ cm}^{-3}$, in gas that has a mean temperature $T \sim 270 \text{ K}$, implying that the Jeans mass at this point is around $350 M_{\odot}$. At the point where we discard the cosmological simulation, the central density is around 10^6 cm^{-3} , and so the collapse has already evolved over two orders of magnitude in density from the point at which the original instability occurred. To ensure that we capture the entire collapsing fragment in our simulations, and to avoid any unphysical boundary effects, we select a spherical region containing $1000 M_{\odot}$ of gas to be re-simulated at higher resolution, and discard the rest of the SPH particles. We also discard the dark matter particles from the simulation at this point, as the further collapse of the gas is dominated by the self-gravity of the gas, rather than the gravitational potential of the dark matter, since it contributes only $\sim 70 M_{\odot}$ in the re-refined region. As such, removing the dark matter only changes the ratio of rotational to gravitational energy by around 7 percent in the region of interest, which is negligible given the variation expected

from cosmic variance.

To account for the effects of the missing gas that should surround this central core, we include a external pressure term that modifies the standard gas-pressure contribution to the Gadget 2 momentum equation,

$$\frac{dv_i}{dt} = - \sum_j m_j \left[f_i \frac{P_i}{\rho_i^2} \nabla_i W_{ij}(h_i) + f_j \frac{P_j}{\rho_j^2} \nabla_i W_{ij}(h_j) \right], \quad (18)$$

by replacing P_i and P_j with $P_i - P_{\text{ext}}$ and $P_j - P_{\text{ext}}$ respectively, where P_{ext} is the external pressure, and all other quantities have the usual meaning (*SI*). The pair-wise nature of the force summation over the SPH neighbors ensures that P_{ext} cancels for particles that are surrounded by other particles. However at the edge of the cloud, the extra pressure term does not disappear, and thus mimics the pressure contribution from a surrounding medium. We use the average density and temperature at the edge of our cloud to define the value of P_{ext} .

In order to allow us to follow the collapse of the gas up to very high densities, it is necessary to substantially increase the resolution. The SPH particle mass in the original cosmological simulation was $0.04 M_{\odot}$, and so the re-simulated region contains 25,000 SPH particles. To increase the resolution, we ‘split’ each of these particles into 100 new SPH particles of lower mass, giving a new particle mass at the beginning of our re-zoomed simulation of $4 \times 10^{-4} M_{\odot}$.

The particle splitting is done by randomly placing the sibling particles inside the smoothing length of the parent particle (*S23, S24, SI4*). Apart from the mass of the siblings, which is 100 times less than that of the parent, they inherit the same values for the entropy, velocities and chemical abundances as their parents, thereby ensuring conservation of mass, linear momentum and energy during the splitting of the particles. Contrary to claims in the literature, splitting the particles does not conserve angular momentum by construction, since the mass distribution changes during the split (and adaptive mess refinement codes suffer from the same problem). However we find the error in the angular momentum introduced during the splitting to be small,

around a percent. This process is repeated several times during the simulation to ensure that the resolution in the collapsing region remains high. However, in these subsequent ‘splits’, the particle mass is only changed by a factor of five at most. In Table S1, we list the densities at which we split the particles, the temperature and local Jeans mass of the gas at the point where splitting occurs, the total mass of gas that undergoes particle splitting at each stage, and the particle mass before and after the splitting. We also list the number of SPH particles per Jeans mass and per Jeans length prior to the splitting, allowing us to demonstrate that we always apply our splitting technique to highly resolved regions.

Our particle splitting technique ensures that particles of significantly different mass (i.e. those with mass ratios greater than 5) never come in contact with one another during the final stages of the simulation, minimizing any potential problems due to the mixing of SPH particles with wildly different masses. The fact that the inner $82 M_{\odot}$ of gas is resolved with a uniform particle mass of $10^{-5} M_{\odot}$ also ensures that the disk is formed by SPH particles that are of equal mass, and we halt the simulations long before any of the higher-mass particles have reached the disk.

At the point of disk fragmentation, our calculations have in excess of 300,000 SPH particles in the disk. Even for mildly self-gravitating disks, this has been shown to be sufficient to provide converged evolution for the angular momentum transport (*S25, S26*). Disks that are more strongly self-gravitating, such as the one we present in this Report, are easier to resolve, as they have a larger scale height.

It should also be stressed that rather than promoting artificial fragmentation, the ‘kernel’ softening employed within Gadget-2 to soften gravitational forces on small scales will tend to suppress fragmentation in unresolved regions rather than promote it (*S17, S27, S28*), since the gravitational forces will be diluted to scales longer than the pressure forces. The high resolution that we employ in this study ensures that we capture all of the fragmentation in the density

Table 1: We summarize here the details of SPH particle masses that result from the ‘particle splitting’ that is used to increase the spatial resolution in our simulation. The quantities given are: the number density at which the resolution is increased; the mean temperature at this density; the corresponding Jeans mass; the mass in the region that is refined; the particle mass, before and after the split; the number of particles resolving a Jeans mass; and the number of particles per Jeans length. For comparison, the bottom two rows show the densities and temperatures associated with the onset of gravitational instability in the disk and the formation of sink particles.

n (cm^{-3})	T (K)	m_J (M_\odot)	M_{split} (M_\odot)	M_{part} (M_\odot)	N_{part}/M_J	$N_{\text{part}}/\lambda_J$
10^6	350	52		0.04	1,304	11
10^6	350	52	1000	4×10^{-4}	130,400	50
10^{10}	750	1.6		4×10^{-4}	4,090	16
10^{10}	750	1.6	336	1×10^{-4}	16,360	25
2×10^{10}	780	1.2		1×10^{-4}	12,269	23
2×10^{10}	780	1.2	178	5×10^{-5}	24,539	29
4×10^{10}	790	0.880		5×10^{-5}	17,687	26
4×10^{10}	790	0.880	82	1×10^{-5}	88,433	44
10^{14}	1200	0.033		1×10^{-5}	3,311	15
10^{17}	1400	0.001		1×10^{-5}	132	5

regime in which we have a reliable thermodynamic model for the gas, while in the density regime in which our thermodynamical model begins to break down (i.e. $n > 10^{17} \text{ cm}^{-3}$), the gas is stable to further fragmentation.

3 State of the cloud at the onset of star formation

One potential concern about our findings is that since we have examined only a single realization of primordial protostellar collapse, we may be obtaining results that are not typical of Population III star formation in general. If the minihalo that we have selected to examine is unusual in some way, then the results that we have obtained from it may be misleading. Ultimately, this is a point that will need to be addressed by performing a large set of simulations along the lines that we

have laid out here, allowing many different realizations to be examined, but at present we do not have sufficient computational resources for such a large-scale study. However, as we argue in the main article, we can gain confidence that our simulated halo is not atypical by comparing its properties to those reported in other studies of Population III star formation.

As mentioned above, the initial gas distribution for our high resolution SPH simulation was taken from a minihalo with a dark matter virial mass of $3.3 \times 10^5 M_\odot$ and a dimensionless spin parameter $\lambda = 0.034$. Runaway gravitational collapse of gas within the minihalo occurred at a redshift $z \sim 17$. For comparison, the halos investigated in two of the most recent high-resolution studies of Population III star formation (*S14*, *S29*) had masses of $5 \times 10^5 M_\odot$ and $5.8 \times 10^5 M_\odot$, respectively, and collapsed at redshifts $z = 14$ and $z = 19$, respectively. Our halo mass is therefore slightly smaller than these previous values, while our collapse redshift is well within the range found in previous work. Our halo spin parameter is slightly smaller than the value of $\lambda = 0.042$ quoted in Turk et al. (*S29*), but lies very close to the mean of the spin parameter distribution found in previous studies of high-redshift dark matter halos (*S30*, *S31*).

We can also compare the state of the gas immediately prior to the formation of the first sink particle with previously reported results. In Figure S8, we show plots of the enclosed mass M_{enc} and specific angular momentum L of the gas as a function of distance from the centre of the collapse (left-hand panels), and of the number density n and radial velocity v_{radial} of the gas as a function of the enclosed gas mass (right-hand panels). If we compare these radial profiles to those reported in previous high-resolution studies (*S5*, *S10*, *S14*, *S29*), we find reasonable agreement. We recover the standard $\rho \propto r^{-2.2}$ density profile at radii greater than a few AU, and masses above $0.1 M_\odot$. Our values for the specific angular momentum agree very well with the values reported elsewhere (*S5*, *S10*), demonstrating that our gas is not rotating artificially rapidly. We also recover a similar infall velocity profile as in previous studies, with a peak value of about 2.5 km s^{-1} , again in good agreement with previously reported results (*S5*, *S14*).

We do not have sufficient resolution to recover the post-shock, sub-AU scale infall visible in Fig. 3B of Yoshida et al. (S14): this would occur within the region that is represented by our central sink particle.

In Figure S9, we show the radial profile of the three components of the angular momentum vector at a point in the cloud’s evolution just before the creation of the first sink particle. The fact that the relative magnitudes of each component remain constant over such a large distance (and enclosed mass) in the cloud shows that the mass shells are, for the most part, rotating around a common axis. Only as the enclosed mass approaches a value roughly comparable to the original Jeans mass in the minihalo, $M_{J,\text{init}} = 350 M_{\odot}$, do we see a significant change in the orientation of the angular momentum vector. This shows that the collapsing region had a well defined rotation axis, while the large-scale motions in the minihalo were much more chaotic. It would be interesting to compare these results to those from previous studies, but to the best of our knowledge, the required data is not available in the astrophysical literature.

We have also examined how the product of the mean angular velocity Ω and the local dynamical time $t_{\text{dyn}} = 1/\sqrt{4\pi G\rho}$ evolves as we move away from the site where the first protostar forms (Figure S10). Yoshida et al. (S14) measured this for the central $0.01 M_{\odot}$ of gas in their simulation at the point at which they could no longer follow the evolution of the system, and found a value $\Omega t_{\text{dyn}} = 0.25$, in good agreement with our own results.

Finally, we have also examined the H_2 distribution in the cloud just before the formation of the first sink particle. In Figure 11, we show how the H_2 fraction (defined here as the ratio of the H_2 number density n_{H_2} to the number density of hydrogen nuclei, n) varies as a function of n . We see that the transition from atomic to molecular hydrogen due to three-body H_2 formation occurs at a density of roughly 10^{10} cm^{-3} , in line with the finding of previous studies that have used the same three-body H_2 formation rate coefficient (S5, S29).

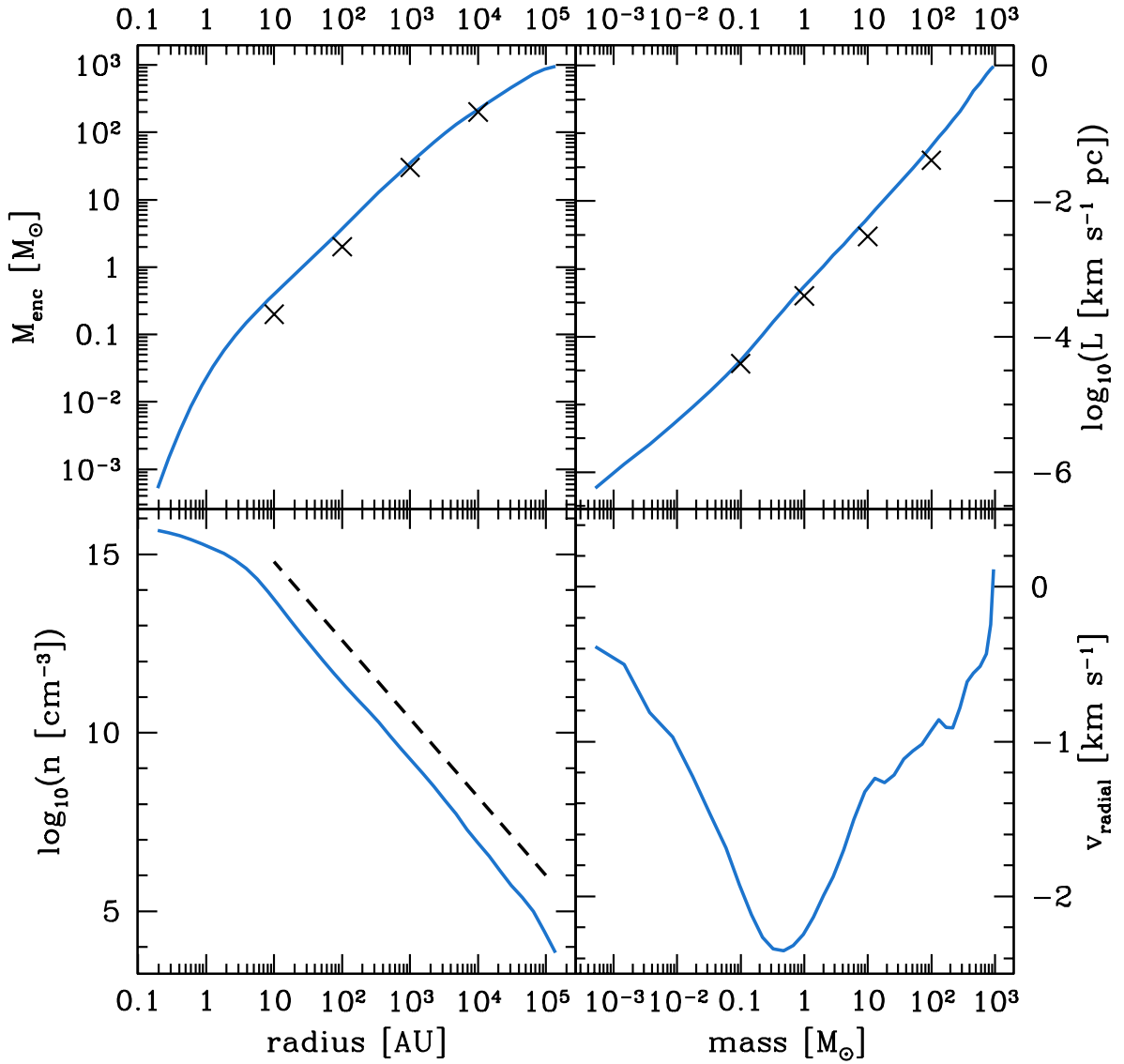


Figure 8: *Upper left panel:* mass enclosed as a function of the radial distance from the densest point in the simulation, plotted just before the formation of the first sink particle. The black crosses represent the corresponding values in the simulation presented by Abel et al. (S5). *Upper right panel:* spherically averaged value of the specific angular momentum, L , plotted at the same time. Crosses represent the values of L for the indicated enclosed masses in the simulation presented by Abel et al. (S5). *Lower left panel:* spherically averaged number density profile at the same time, plotted as a function of the enclosed mass. To help guide the eye, the dashed line represents the $\rho \propto r^{-2.2}$ slope found in previous simulations of Population III star formation. *Lower right panel:* spherically averaged radial velocity profile

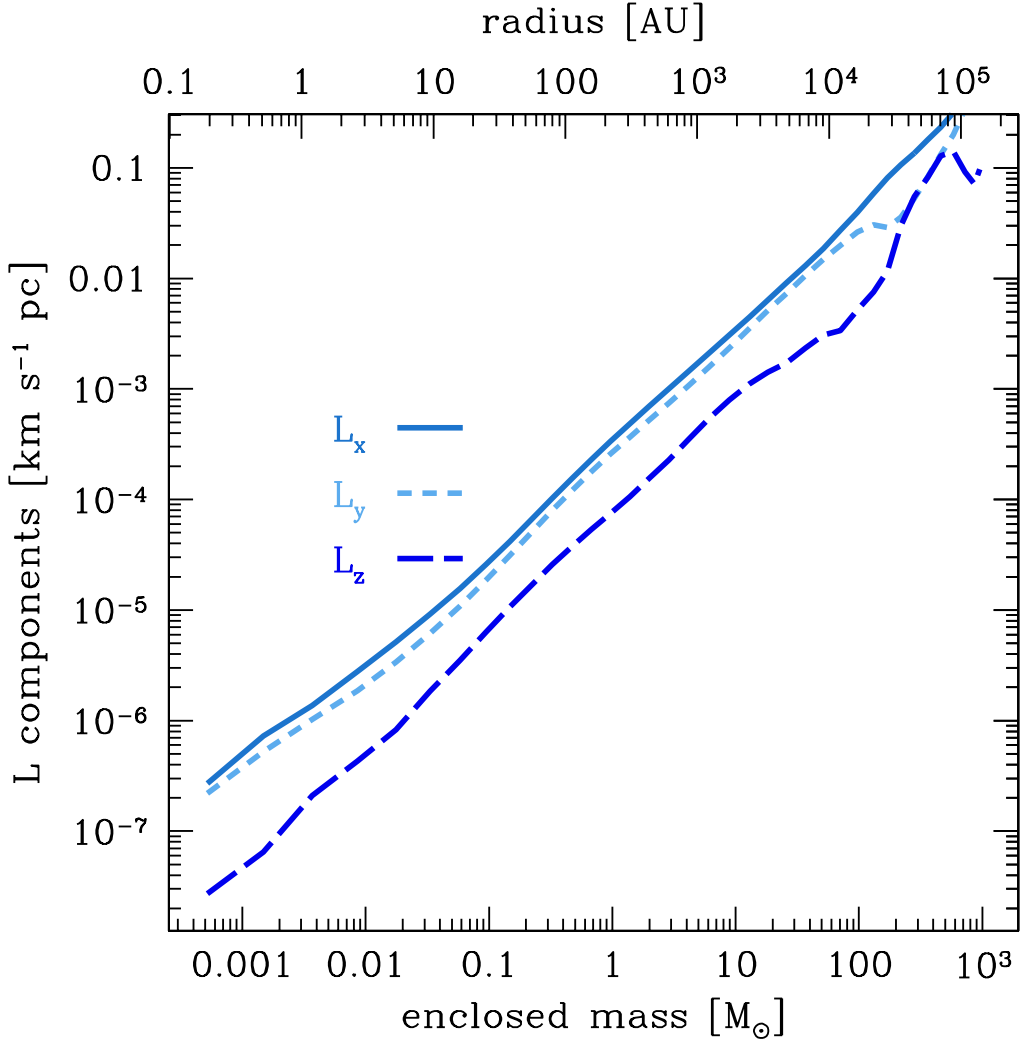


Figure 9: The magnitudes of the individual components of the specific angular momentum vector in each shell, plotted as a function of both enclosed mass and radius. The values are mass-weighted and are taken from a point in the calculation immediately prior to the formation of the first sink particle. The angular momentum is calculated with respect to the densest point in the gas.

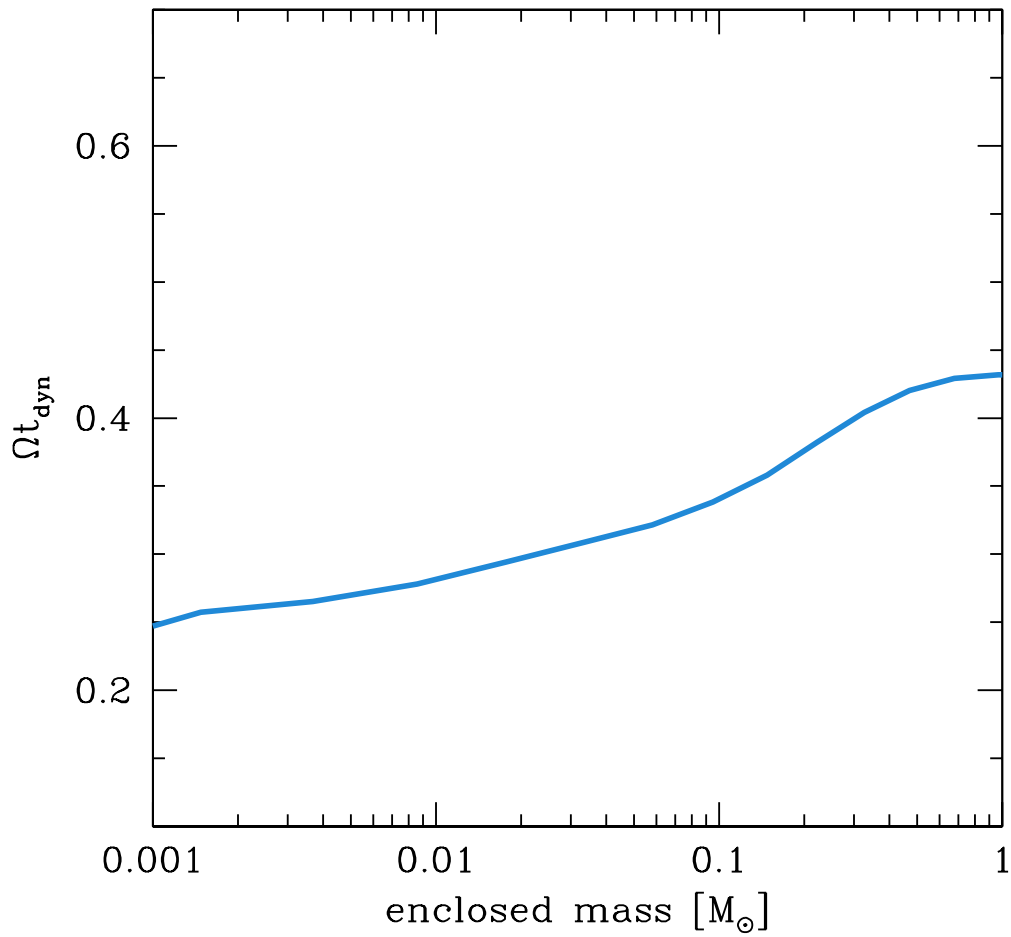


Figure 10: The product of the mean angular velocity Ω and the local dynamical time $t_{\text{dyn}} = 1/\sqrt{4\pi G\rho}$, plotted as a function of the enclosed gas mass, at a point in the calculation immediately prior to the formation of the first sink particle.

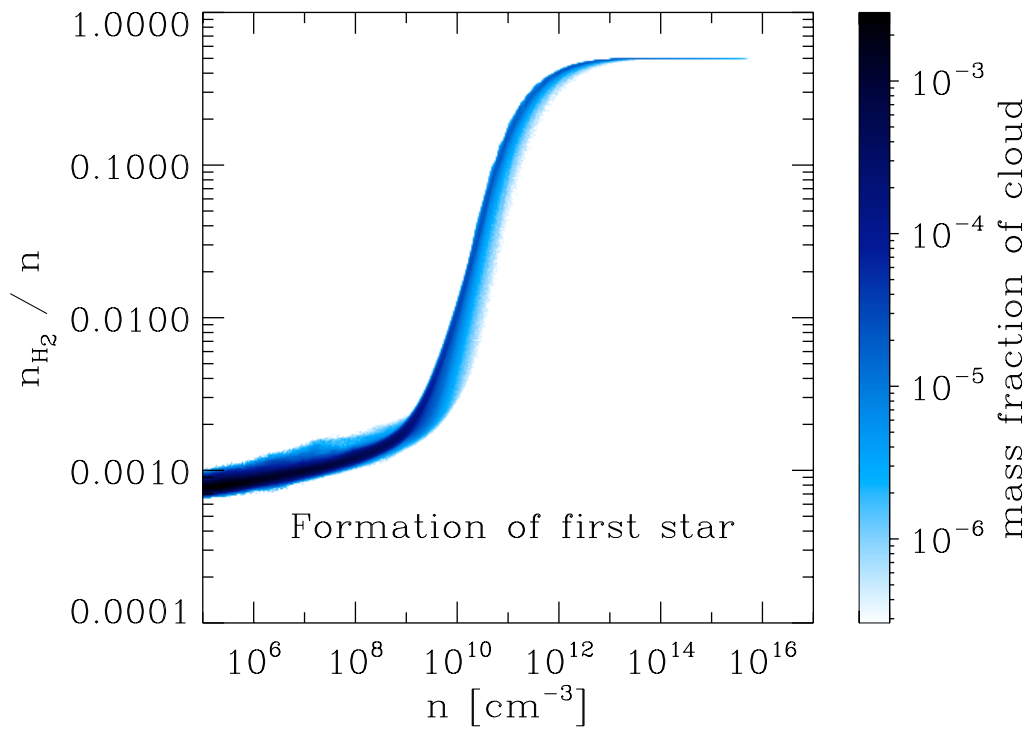


Figure 11: Ratio of the H_2 number density, n_{H_2} , to the number density of hydrogen nuclei, n , plotted as a function of n , at a time immediately prior to the formation of the first sink particle. Note that a value $n_{\text{H}_2}/n = 0.5$ indicates fully molecular gas.

4 Sensitivity to the choice of accretion rate

Once gas begins to accumulate in an accretion disk around the initial sink particle, its subsequent evolution will depend to some extent upon its temperature, and hence on the degree to which it is heated by radiation from the accreting protostar. As already discussed in Section 1, one of the difficulties involved in a self-consistent determination of the accretion luminosity of the protostar lies in establishing an appropriately time-averaged estimate for the protostellar accretion rate that is insensitive to the particle-based nature of SPH. In our present study, we calculate the instantaneous accretion rate onto each protostar by computing a smoothed average of the accretion rate over the previous ten years. This procedure yields a reasonable estimate of the true accretion rate, as Figure S6 demonstrates, but nevertheless it remains an approximation. It is therefore informative to examine the sensitivity of our results to the value of the protostellar accretion rate, in order to help us understand whether the approximation that we are making is likely to be a significant source of uncertainty.

To address this issue, we have examined the results of two additional simulations, performed using fixed values of $\dot{M}_* = 10^{-2} M_\odot \text{yr}^{-1}$ and $\dot{M}_* = 10^{-3} M_\odot \text{yr}^{-1}$, respectively, for the protostellar accretion rate used to compute the accretion luminosity of the protostar. As we can see from Figure S6, these two values bracket the true accretion rate during the period of time covered by our simulations. We find evidence for disk fragmentation in both of these simulations. When the accretion rate onto the central protostar is low, and hence the accretion luminosity is less effective, fragmentation occurs more rapidly than when the accretion rate is high. In the $\dot{M}_* = 10^{-3} M_\odot \text{yr}^{-1}$ simulation, it takes only 105 years before the disk fragments to form a second sink particle, whereas in the higher \dot{M}_* simulation it takes 274 years for this to happen. Furthermore, when the accretion rate is low, fragmentation occurs closer to the central protostar than when the accretion rate is high, as can be seen by comparing Figures S12 and

S13 (although note the difference in the linear scale of these two figures). Nevertheless, in both cases, the general features of the fragmentation are the same: the symmetry in the spiral pattern breaks and one arm becomes gravitationally unstable, with part collapsing to form a new protostar. The second arm follows quickly after it (no more than a few tens of years in both cases), with the result that 4 to 5 stars are formed within a few years of the onset of fragmentation in the disk.

If we compare the results of these simulations with the results of the simulation that used a more self-consistent determination of \dot{M}_* , we see that the behaviour of the latter closely resembles that found in the $\dot{M}_* = 10^{-3} M_\odot \text{yr}^{-1}$ simulation, with fragmentation occurring relatively quickly at a distance of roughly 20 AU from the central protostar. This result is not particularly surprising, given that the true accretion rate onto the central protostar is only slightly larger than $10^{-3} M_\odot \text{yr}^{-1}$ at the point at which the disk fragments (Figure S6), but the fact that we still find that fragmentation of the disk occurs even when the adopted accretion rate is substantially larger than this argues that any small uncertainties in our determination of \dot{M}_* are unlikely to be significantly influencing our results.

In Figure S14, we compare the surface density, temperature, H₂ fraction and Toomre stability parameter for the disks in our three simulations at the point at which the second sink particle forms in each simulation. We see that when \dot{M}_* is small, the accretion disk is systematically colder at all radii $R < 40$ AU, and is also significantly denser within the central 5 AU, although at larger radii the disk surface densities do not differ by a large factor. The higher central temperature in the high \dot{M}_* simulation causes a pronounced central dip in the H₂ fraction (defined here as n_{H_2}/n , which means that a value of 0.5 corresponds to fully molecular gas). This dip is almost absent in the other two simulations. Comparing the Toomre parameter of the three disks, we see that they all have $Q \sim 1$ at radii greater than about 5–10 AU, indicating that in each case, the disk is strongly self-gravitating. It is therefore not surprising that we find fragmentation in

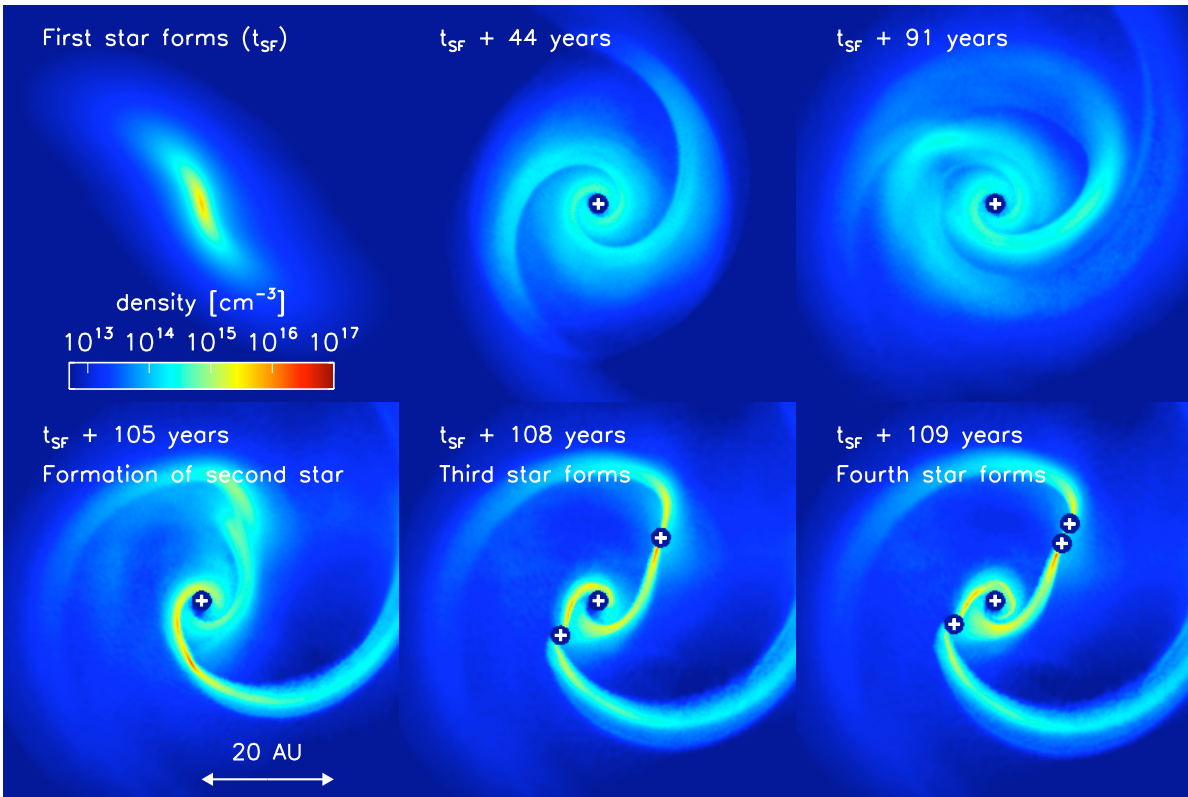


Figure 12: The evolution of the density in the $\dot{M}_* = 10^{-3} M_\odot \text{ yr}^{-1}$ simulation, showing the build-up of the accretion disk around the central protostar. Note that the scale and color table are different from those used in Figure 1 in the main article.

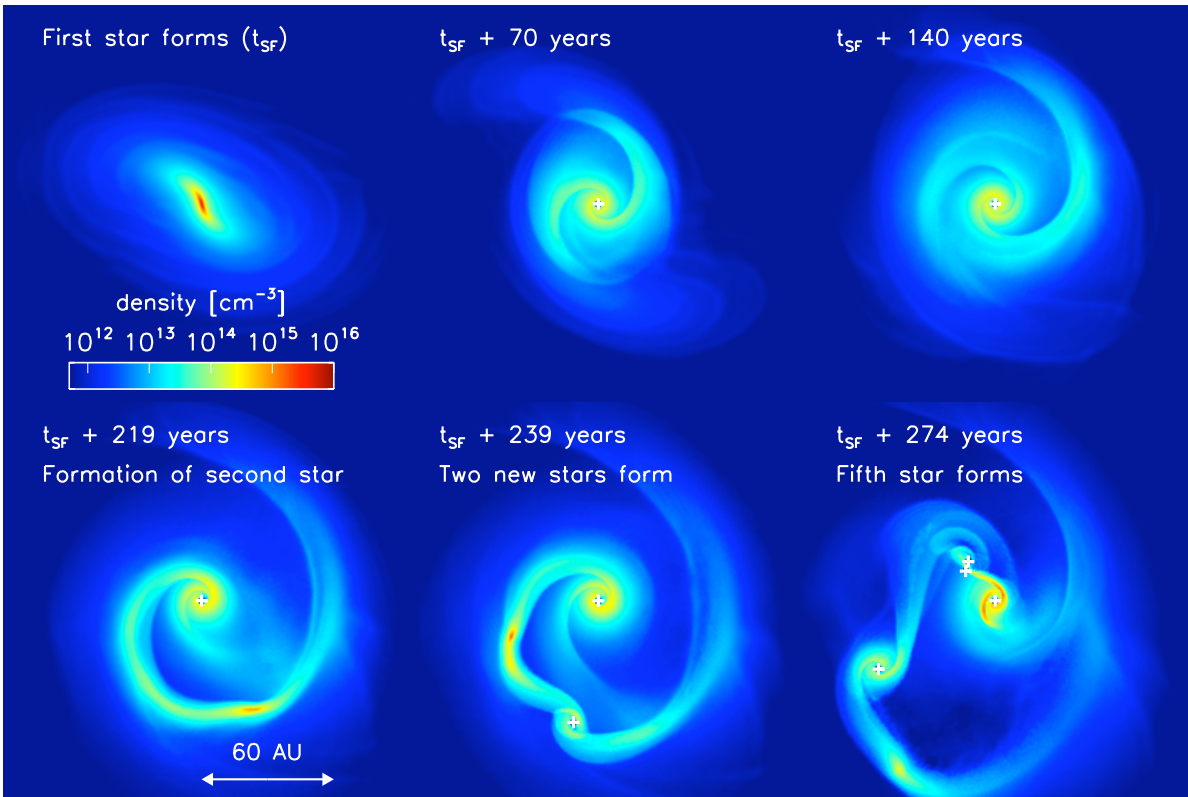


Figure 13: The evolution of the density in the $\dot{M}_* = 10^{-2} M_{\odot} \text{ yr}^{-1}$ simulation, showing the build-up of the accretion disk around the central protostar. Note that the scale is different to that used in Figure 1 in the main article.

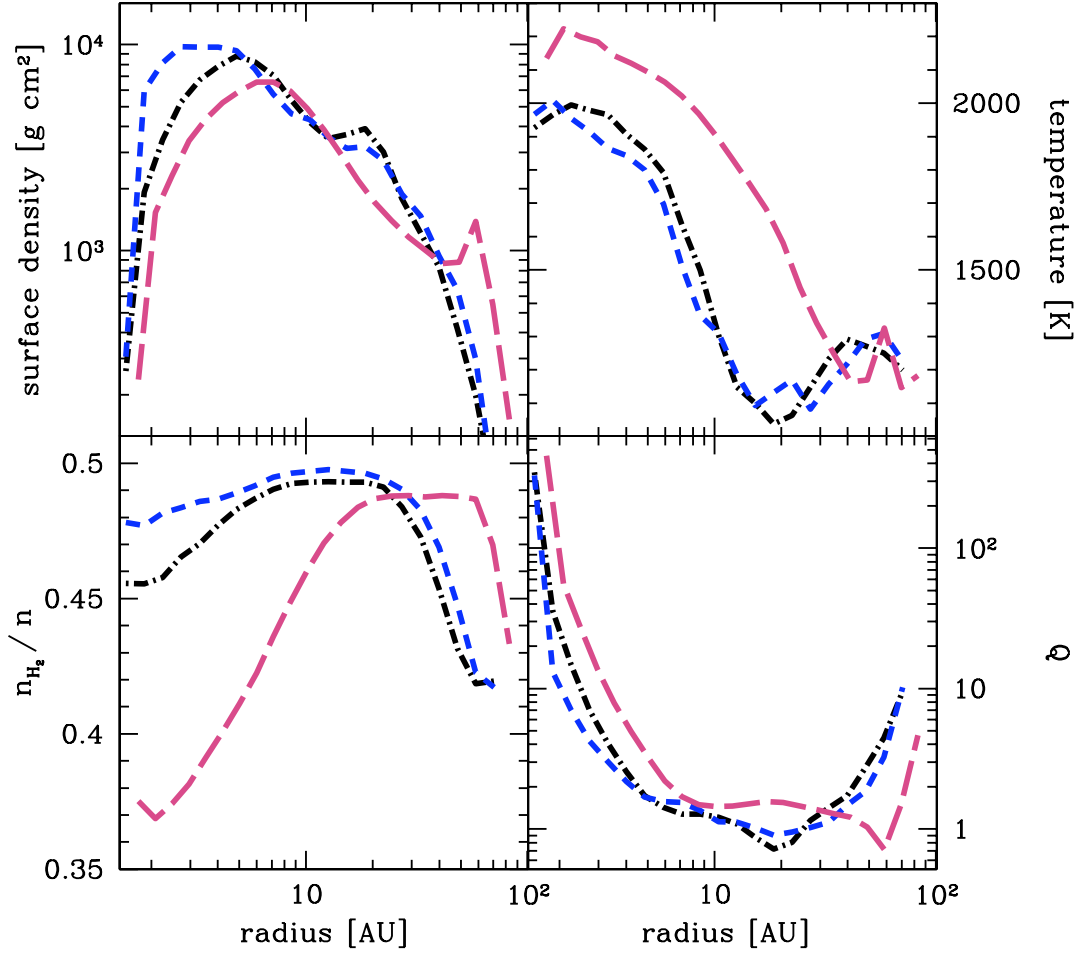


Figure 14: Radially averaged disk properties, measured at a point immediately prior to the formation of a second sink particle, in simulations with the live accretion rate (black, dot-dashed line), $\dot{M}_* = 10^{-3} M_\odot \text{ yr}^{-1}$ (blue, short-dashed line) and $\dot{M}_* = 10^{-2} M_\odot \text{ yr}^{-1}$ (pink, long-dashed line). In the low fixed \dot{M}_* simulation, the second sink forms at $t_{\text{SF}} + 105$ years, and in the high fixed \dot{M}_* simulation, the second sink forms at $t_{\text{SF}} + 274$ years, where t_{SF} denotes the time at which the initial sink particle formed. In the simulation with the live accretion rate, the second sink particle forms at $t_{\text{SF}} + 91$ years, a little earlier than in the low fixed accretion rate calculation.

all three simulations. In fact, the conditions in the disk and infalling envelope are similar to those found to lead to fragmentation in a recent study of present-day star formation (S32).

5 Protostellar masses and accretion rates

In Figure S15, we show how the masses of the protostars evolve over the first 120 years of the simulation and how the accretion rates onto the protostars vary with time. The first point to note is that all of the protostars have a mass of roughly $3 \times 10^{-2} M_{\odot}$ when they form. This is not particularly surprising, as this mass scale is simply set by the Jeans mass within the protostellar accretion disk. However, accretion from their surroundings rapidly increases the protostellar masses, which typically exceed $0.1 M_{\odot}$ within only 10–20 years of their formation. Another point to note is that although accretion onto the central protostar initially proceeds in a fairly smooth manner, the onset of fragmentation in the disk produces strong gravitational torques that allow more mass to flow into the central protostar, but that also cause the accretion rate to become far more variable. Similarly, the complex gravitational interactions between the new protostars and the disk also cause the accretion rates onto these protostars to vary strongly with time.

As the disk breaks up, the computational expense involved in following its further evolution becomes very large, and so for the present we have been forced to terminate our simulations once four or five protostars have formed. At the point at which we stop the simulations, there is roughly an order of magnitude difference between the mass of the most massive and least massive protostars, but given the high rates at which all of the protostars are accreting gas, plus the fact that at this point less than 0.1% of the available gas has been accreted, we cannot state with any certainty what the final spread in stellar masses will be, or indeed how many protostars will ultimately be formed.

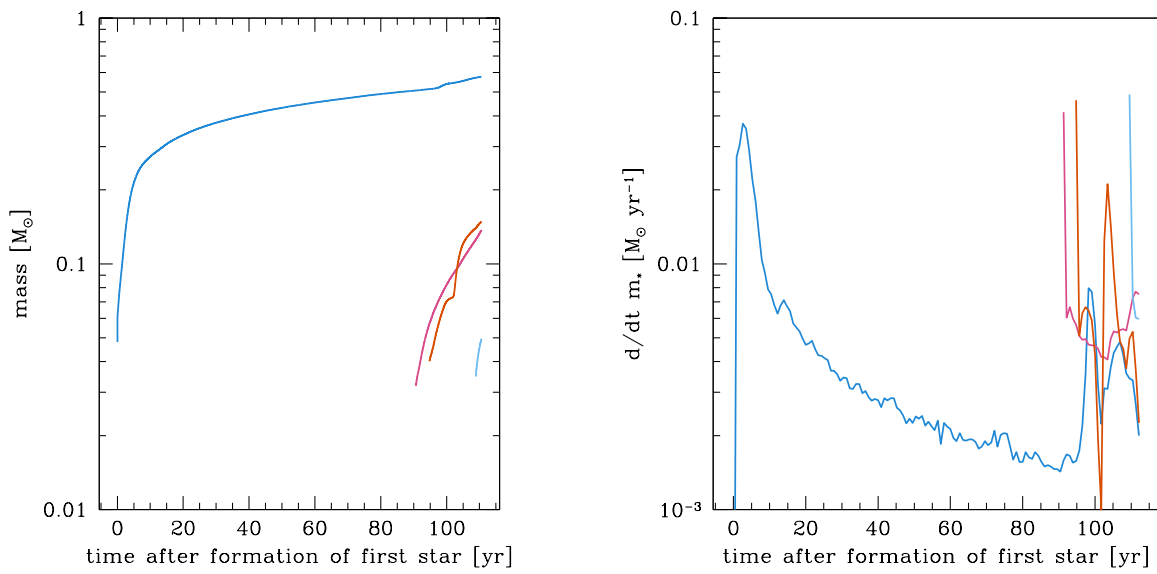


Figure 15: *Left panel:* The evolution with time of the masses of the sink particles. *Right panel:* The accretion rates onto the individual sinks. Once the disk begins to fragment, the strong gravitational torques allow more mass to flow onto the central protostar. However, the complex interactions between the individual sinks, and between the sinks and the disk cause the accretion rates of all of the sinks to become highly variable.

6 Rotational support of the accretion disk

The velocity and mass profiles in the protostellar disk at the point of fragmentation are shown in Fig S16. We see that despite the strong spiral features, the disk is essentially Keplerian. We also see that a substantial fraction of the disk is moving *away* from the central protostar as the new fragment forms, demonstrating that the new protostar is forming in a region that is directly responsible for the transport of angular momentum through the disk. In fact, the fragmentation occurs at a radius of about 20 AU from the central protostar: roughly the point at which the material moving outwards collides with the gas coming in from the envelope.

The mass profile of the protostar-disk system is also shown in Fig S16. We see that the mass enclosed by the disk at 20 AU is roughly $2 M_{\odot}$, while the mass in the central protostar at this time is only around $0.5 M_{\odot}$. The disk is therefore significantly more massive than the central protostar, a feature commonly reported for the early phases of protostellar mass growth in the simulations of present-day star formation (S33).

7 Thermodynamics of the accretion disk

There are two main criteria that an accretion disk must satisfy before it is able to undergo gravitational fragmentation – the Toomre criterion discussed in the main article, and the Gammie criterion, which states that the thermal timescale of the gas in the disk must be a small fraction of the orbital timescale (S34)

$$t_{\text{thermal}} \leq 3\Omega^{-1} \equiv \frac{3}{2\pi} t_{\text{orbital}}, \quad (19)$$

where $t_{\text{thermal}} = e/\Lambda$, where e is the internal energy density and Λ is the volumetric cooling (or heating) rate, Ω is the rotation frequency of the disk, and $t_{\text{orbital}} = 2\pi/\Omega$. If the thermal timescale does not satisfy the Gammie criterion, then gravitationally collapsing gas in the disk

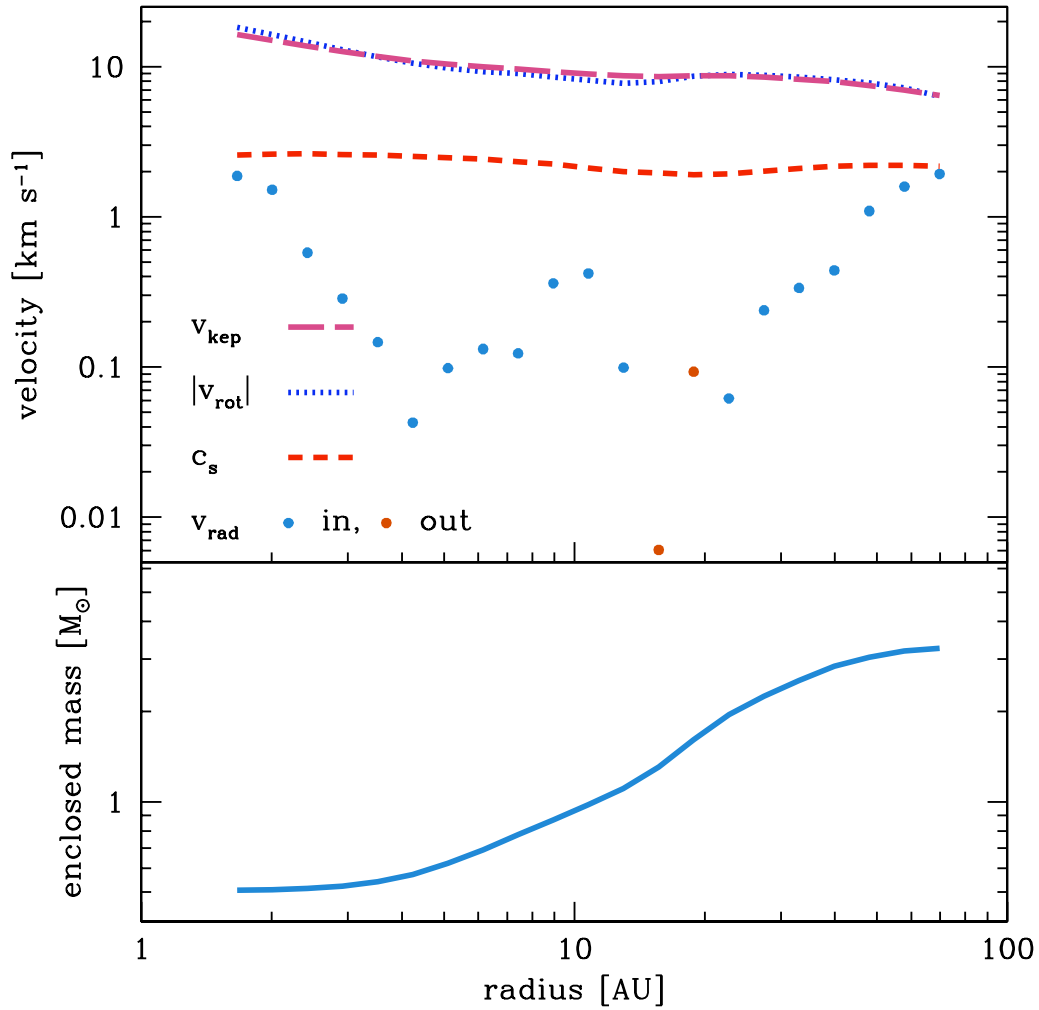


Figure 16: *Upper panel:* radial velocity profiles in the plane of the disk, along with the sound speed of gas, at a point in the simulation just before the disk fragments to form a second protostar. Regions of the disk that are moving towards the central star are shown by blue dots, while those those moving away are shown in red. *Lower panel:* Mass profile of the protostar-disk system just before fragmentation.

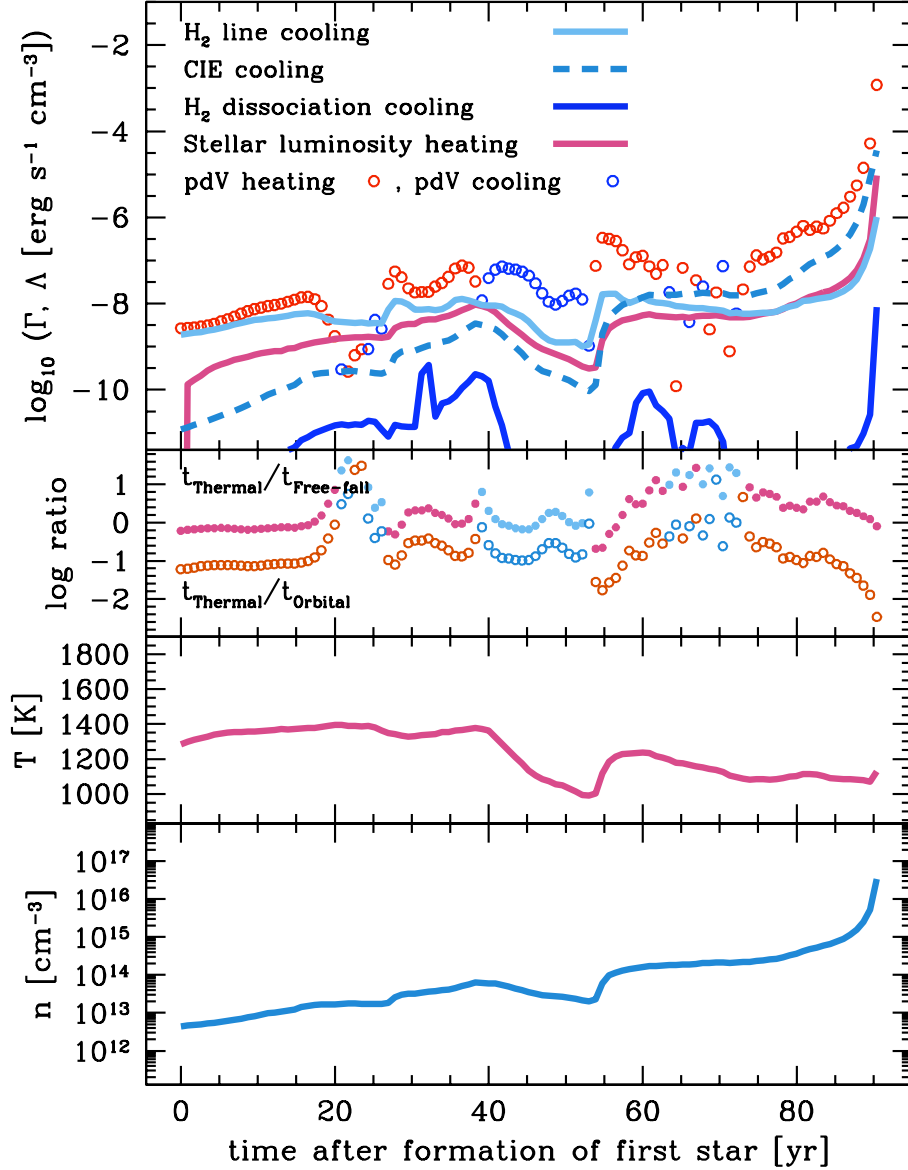


Figure 17: (a) Dominant heating and cooling processes in the gas that forms the second sink particle. (b) Upper line: ratio of the thermal timescale, t_{thermal} , to the free-fall timescale, t_{ff} , for the gas that forms the second sink particle. Periods when the gas is cooling are indicated in blue, while periods when the gas is heating are indicated in red. Lower line: ratio of t_{thermal} to the orbital timescale, t_{orbital} , for the same set of SPH particles (c) Temperature evolution of the gas that forms the second sink (d) Density evolution of the gas that forms the second sink

will undergo a thermal bounce and then be sheared apart by the disk rotation, rather than continuing to collapse. It is therefore important to understand the thermal evolution of the material in the disk, and to verify that the gas which fragments does indeed satisfy the Gammie criterion.

To do this, we have harnessed the Lagrangian nature of SPH. We first identify the SPH particle that finds itself at the center of the region in the disk that collapses to form the second protostar. This is the particle that is turned into a sink particle, once it (and its neighbors) pass the tests described in Section 1. We then go back to a point in the simulation just after the central protostar is formed, and follow the evolution of this particle by computing the mean properties of the gas as seen by the particle and its 50 nearest neighbors at many different instances in the life of the disk. It is this evolution that is shown in Figure S17.

We found that the gas which formed our second sink particle underwent several orbits in the disk prior to becoming gravitationally unstable, passing into and out of the spiral density wave pattern present in the disk. Gas entering the spiral density wave pattern was compressed, while gas exiting it was rarefied, as can be seen from panels 3 and 4 of Figure S17. During periods of compression, the dynamical heat input (red circles in panel (a) of Figure S17) was balanced primarily by radiative cooling through H_2 line emission (pale blue line in panel (a) of Figure S17), even though the strongest of the H_2 lines all had significant optical depths at this point in the calculation. In comparison, cooling from H_2 collision-induced emission (CIE; blue dashed line in panel (a) of Figure S17) made only a minor contribution to the dissipation of energy from the disk throughout most of the simulation. The other cooling process included in the Figure, H_2 collisional dissociation cooling (dark blue line in panel (a) of Figure S17), is generally negligible for the material in the disk. However, the exponential temperature dependence of the collisional dissociation rate means that it rapidly becomes more important as the temperature rises.

Once runaway gravitational collapse sets in at $t \sim 90$ yr, the relative importance of the

three main cooling processes changes. As the density and temperature of the gas increase, all three processes yield higher volumetric cooling rates. However, the rate of increase in the H₂ line cooling rate is slow, owing to the effects of the high line opacity, and so it is quickly overtaken by CIE cooling. At the time of the last output dump before the formation of the sink particle, H₂ collisional dissociation cooling has less influence than H₂ line cooling or CIE cooling, and the gas remains almost entirely molecular, with an atomic hydrogen fraction of order 10⁻³. However, it is plain that the importance of H₂ collisional dissociation cooling is increasing rapidly at this point, and we expect it to become the dominant process limiting the rate of increase of the temperature of the collapsing gas at higher densities. This is important, as this is a non-radiative process, and hence one that will be unaffected by the increasing opacity of the collapsing gas. Although we do not follow the details of the collapse beyond our sink particle creation density, it is reasonable to assume that the collapse will proceed in a quasi-isothermal fashion for as long as there remains H₂ available to dissociate, just as in simulations of present-day star formation (*S35, S36*), or high dynamical range simulations of primordial star formation (*S14*). Only once the H₂ content of the collapsing gas is exhausted will the collapse become adiabatic.

We can also draw an important conclusion from Figure S17 regarding the importance of accretion luminosity heating in determining the temperature evolution of the gravitationally unstable gas. It is clear from panel (a) of Figure S17 that the accretion luminosity generally plays only a minor role in heating the gas, in comparison to compressional and viscous heating in the disk, dominating only when these terms are small or absent. Since our numerical treatment of the accretion luminosity heating is designed to maximize its effects, we can be confident of finding the same result were we to use a more accurate treatment of the accretion luminosity feedback. We can therefore also be confident that radiative feedback from the first star to form does not suppress fragmentation in the disk at this stage in the lifetime of the system. We can-

not, of course, rule out significant feedback effects later in the lifetime of the disk, when the mass of the central sink will be larger, but these lie beyond the scope of our present study.

As far as the Gammie criterion is concerned, we can see from panel (b) of Figure S17 that this is satisfied for almost the whole period plotted. Typically, $t_{\text{thermal}} \sim 0.1 t_{\text{orbital}}$, increasing above this value only occasionally. Most importantly, $t_{\text{thermal}}/t_{\text{orbital}}$ becomes small once the gas begins to undergo runaway gravitational collapse, decreasing to roughly $t_{\text{thermal}}/t_{\text{orbital}} \sim 0.01$ by the end of the simulation. In contrast, we note that the gas in the disk finds the standard Rees & Ostriker criterion for ongoing gravitational collapse (S37), namely that $t_{\text{ff}} > t_{\text{thermal}}$, more difficult to satisfy. It is this condition that helps to maintain the overall global stability in the disk.

Finally, the results presented here allow us to understand why our conclusions regarding the stability of Population III accretion disks differ significantly from those of the previous analytical studies (S20, S38, S39). Figure S17 demonstrates that H_2 line cooling plays a hugely important role in the thermal balance of the disk, allowing the disk material to remain relatively cold, with a temperature of $T \sim 1000\text{--}2000$ K. However, this process was not included in any of these previous analytical studies. They therefore find much higher equilibrium temperatures for the gas in the disk. Neglect of H_2 bound-free opacity means that these studies predict inner disk temperatures $T \sim 6000$ K or more, the temperature at which H^- ions first become a major source of opacity. At a temperature of 6000 K, the molecular content of the gas is negligible, and so the predicted mean molecular weight of the gas in these models also differs by almost a factor of two from the value in our cold disks. Together, these effects lead to a significantly higher predicted sound-speed for the disk, and hence also a higher Toomre parameter Q . Our simulated disks are already marginally stable, and it is likely that a global increase in Q by a factor of a few would render them completely stable against fragmentation. The difference between the results of these earlier analytical studies and our simulations can therefore be understood as a

direct consequence of the difference in the input physics, and underscores the importance of properly accounting for the H₂ line cooling.

8 Potential impact of magnetic fields

Magnetic fields in the early universe are usually assumed to be extremely weak and their potential influence on the gas dynamics is neglected in most numerical simulations of Population III star formation (*S40*). Upper limits on the field strength can be derived from the cosmic microwave background (*S41*), from big-bang nucleosynthesis (*S42, S43*), from modeling the reionization history (*S44*), or from the 21 cm line (*S45*). Typical values lie around 10^{-9} G in comoving units.

Although a variety of physical processes have been proposed for the creation of a seed magnetic field during inflation, for example via electroweak or QCD phase transitions (*S46*), most studies conclude that the dominant contribution to the magnetic field strength comes from astrophysical processes after recombination. The Biermann battery has been proposed to generate fields of the order of 10^{-18} G in the intergalactic medium at a redshift of $z \approx 20$ (*S47*). This field could be amplified further via the Weibel instability in shocks (*S48, S49*). The most likely mechanism for field amplification, however, is the dynamo process (*S50*). Indeed, two recent studies (*S51, S52*) conclude that the presence of a small-scale turbulent dynamo is able to increase the field strength by many orders of magnitude during the collapse of primordial gas clouds. Once a disk has formed, the large-scale dynamo and the magnetorotational instability may also become important (*S38, S53*). In addition, the presence of coherent fields could launch jets and outflows (*S54, S55*).

From studies of low-mass star formation in the present day, we know that the presence of magnetic fields with field strengths close to the equipartition value can effectively redistribute angular momentum via a process called magnetic braking (*S56, S57*) and can thereby influence

the fragmentation behavior (S58, S59). However, this requires the presence of coherent rotational motions in the disk. Calculations of massive star formation in the solar neighborhood with and without radiative feedback (S60, S61, S62) show that the disk around the central protostar quickly fragments to build up a cluster of stars, resulting in extremely complex and chaotic gas flows. It is likely that this will reduce the effectiveness with which magnetic fields can redistribute angular momentum and drive magnetic tower flows. As a consequence, the fragmentation behavior of the accretion disk around high-mass stars is not changed much by the presence of the field. As the disks studied in present-day high-mass star formation calculations are similar in nature to the Population III accretion disks modeled in our simulations, we feel confident that correctly accounting for the presence of primordial magnetic fields would not change our conclusions.

References

- S1. V. Springel, *Mon. Not. R. Astron. Soc.*, **364**, 1105–1134 (2005).
- S2. M. R. Bate, I. A. Bonnell, N. M. Price, *Mon. Not. R. Astron. Soc.*, **277**, 362–376 (1995).
- S3. A.-K. Jappsen, R. S. Klessen, R. B. Larson, Y. Li, M.-M. Mac Low, *Astron. Astrophys.*, **435**, 611–623 (2005).
- S4. P. C. Clark, S. C. O. Glover, R. S. Klessen, & V. Bromm, *Astrophys. J.*, in press; (available at <http://arxiv.org/abs/1006.1508>).
- S5. T. Abel, G. Bryan, M. L. Norman, *Science*, **295**, 93–98 (2002).
- S6. S. C. O. Glover, in *First Stars III*, B. W. O’Shea, A. Heger, T. Abel, Eds. (AIP, New York, 2008), pp. 25–29.
- S7. S. C. O. Glover, D. W. Savin, *Mon. Not. R. Astron. Soc.*, **393**, 911 (2009)

- S8. D. R. Flower, G. J. Harris, *Mon. Not. R. Astron. Soc.*, **377**, 705 (2007)
- S9. S. C. O. Glover, T. Abel, *Mon. Not. R. Astron. Soc.*, **388**, 1627–1651 (2008).
- S10. N. Yoshida, K. Omukai, L. Hernquist, T. Abel, *Astrophys. J.*, **652**, 6–25 (2006)
- S11. D. A. Neufeld, M. J. Kaufman, *Astrophys. J.*, **418**, 263–272 (1993)
- S12. E. Ripamonti, T. Abel, *Mon. Not. R. Astron. Soc.*, **348**, 1019–1034 (2004)
- S13. E. Ripamonti, F. Haardt, A. Ferrara, M. Colpi, *Mon. Not. R. Astron. Soc.*, **334**, 401–418 (2002)
- S14. N. Yoshida, K. Omukai, L. Hernquist, *Science*, **321**, 669–671 (2008)
- S15. M. Mayer, W. J. Duschl, *Mon. Not. R. Astron. Soc.*, **358**, 614–631 (2005)
- S16. D. C. Black, P. Bodenheimer, *Astrophys. J.*, **199**, 619–632 (1975)
- S17. M. R. Bate, A. Burkert, *Mon. Not. R. Astron. Soc.*, **288**, 1060–1072 (1997)
- S18. T. Hosokawa, K. Omukai, *Astrophys. J.*, **691**, 823–846 (2009)
- S19. S. W. Stahler, F. Palla, E. E. Salpeter, *Astrophys. J.*, **302**, 590–605 (1986)
- S20. J. C. Tan, C. F. McKee, *Astrophys. J.*, **603**, 383–400 (2004)
- S21. D. N. Spergel et al., *Astrophys. J. Suppl. Ser.*, **148**, 175–194 (2003)
- S22. T. H. Greif, S. C. O. Glover, V. Bromm, R. S. Klessen, *Astrophys. J.*, **716**, 510–520 (2010)
- S23. S. Kitsionas, A. P. Whitworth, *Mon. Not. R. Astron. Soc.*, **330**, 129–136 (2002)
- S24. V., Bromm, V., A., Loeb, *Astrophys. J.*, **596**, 34–46 (2003)

- S25. G. Lodato, W. K. M. Rice, *Mon. Not. R. Astron. Soc.*, **351**, 630–642 (2004)
- S26. G. Lodato, W. K. M. Rice, *Mon. Not. R. Astron. Soc.*, **358**, 1489–1500 (2005)
- S27. A. P. Whitworth, *Mon. Not. R. Astron. Soc.*, **296**, 442–444 (1998)
- S28. D. A. Hubber, S. P. Goodwin, A. P. Whitworth, *Astron. Astrophys.*, **450**, 881–886 (2006)
- S29. M. J. Turk, T. Abel, B. O’Shea, *Science*, **325**, 601–604 (2009)
- S30. H. Jang-Condell, L. Hernquist, *Astrophys. J.*, **548**, 68–78 (2001)
- S31. A. J. Davis, P. Natarajan, *Mon. Not. R. Astron. Soc.*, **407**, 691–703 (2010)
- S32. K. M. Kratter, C. D. Matzner, M. R. Krumholz, R. I. Klein, *Astrophys. J.*, **708**, 1585–1597 (2010)
- S33. R. Banerjee, R. E. Pudritz, L. Holmes, *Mon. Not. R. Astron. Soc.*, **355**, 248–272 (2004)
- S34. C. F. Gammie, *Astrophys. J.*, **553**, 174–183 (2001)
- S35. R. B. Larson, *Mon. Not. R. Astron. Soc.*, **145**, 271–295 (1969)
- S36. H. Masunaga, S. Inutsuka, *Astrophys. J.*, **531**, 350–365 (2000)
- S37. M. J. Rees, J. P. Ostriker, *Mon. Not. R. Astron. Soc.*, **179**, 541–559 (1977)
- S38. J. C. Tan, E. G. Blackman, *Astrophys. J.*, **603**, 401–413 (2004)
- S39. M. Mayer, W. J. Duschl, *Mon. Not. R. Astron. Soc.*, **356**, 1–11 (2005)
- S40. V. Bromm, N. Yoshida, L. Hernquist & C. F. McKee, *Nature*, **459**, 49–54 (2009)
- S41. J. D. Barrow, P. G. Ferreira, J. Silk, *Phys. Rev. Lett.*, **78**, 3610–3613 (1997)

- S42. G. Greenstein, *Nature*, **223**, 938–939 (1969)
- S43. J. J. Matese, R. F. O’Connell, *Astrophys. J.*, **160**, 451–458 (1970)
- S44. D. R. G. Schleicher, R. Banerjee, R. S. Klessen, *Phys. Rev. D*, **78**, 083005 (2008)
- S45. D. R. G. Schleicher, R. Banerjee, R. S. Klessen, *Astrophys. J.*, **692**, 236–245 (2009)
- S46. D. Grasso, H. R. Rubinstein, *Phys. Rep.*, **348**, 163–266 (2001)
- S47. H. Xu, B. W. O’Shea, D. C. Collins, M. L. Norman, H. Li, S. Li, *Astrophys. J.*, **688**, L57–L60 (2008)
- S48. R. Schlickeiser, P. K. Shukla, *Astrophys. J.*, **599**, L57–L60 (2003)
- S49. M. Lazar, R. Schlickeiser, R. Wielebinski, S. Poedts, *Astrophys. J.*, **693**, 1133–1141 (2009)
- S50. R. E. Pudritz, J. Silk, *Astrophys. J.*, **342**, 650–659 (1989)
- S51. D. R. G. Schleicher, R. Banerjee, S. Sur, T. G. Arshakian, R. S. Klessen, R. Beck, M. Spaans, *Astron. Astrophys.*, **522**, A115 (2010)
- S52. S. Sur, D. R. G. Schleicher, R. Banerjee, C. Federrath, R. S. Klessen, *Astrophys. J.*, **721**, L134–L138 (2010)
- S53. J. Silk, M. Langer, *Mon. Not. R. Astron. Soc.*, **371**, 444–450 (2006)
- S54. M. N. Machida, K. Omukai, T. Matsumoto, S.-I. Inutsuka, *Astrophys. J.*, **647**, L1–L4 (2006)
- S55. M. N. Machida, S.-I. Inutsuka, T. Matsumoto, *Astrophys. J.*, **676**, 1088–1108 (2008)
- S56. T. Ch. Mouschovias, E. V. Paleologou, *Astrophys. J.*, **230**, 204–222 (1979)

- S57. P. Hennebelle, A. Ciardi, *Astron. Astrophys.*, **506**, L29–L32 (2009)
- S58. P. Hennebelle, R. Teyssier, *Astron. Astrophys.*, **477**, 25–34 (2008)
- S59. P. Hennebelle, S. Fromang, *Astron. Astrophys.*, **477**, 9–24 (2008)
- S60. M. R. Krumholz, R. I. Klein, C. F. McKee, S. S. R. Offner, A. J. Cunningham, *Science*, **323**, 754–757 (2009)
- S61. T. Peters, R. Banerjee, R. S. Klessen, M.-M. Mac Low, R. Galván-Madrid, E. R. Keto, *Astrophys. J.*, **711**, 1017–1028 (2010)
- S62. T. Peters, R. S. Klessen, M.-M. Mac Low, R. Banerjee, *Astrophys. J.*, **725**, 134–145 (2010)